Design, Construction, and Implementation of a Magnetic Resonance Elastography Actuator for Research Purposes

Emily Rose Triolo,¹ Oleksandr Khegai,² Efe Ozkaya,² Nicholas Rossi,³ Akbar Alipour,² Lazar Fleysher,² Priti Balchandani,² and Mehmet Kurt^{1,2,4}

Magnetic resonance elastography (MRE) is a technique for determining the mechanical response of soft materials using applied harmonic deformation of the material and a motion-sensitive magnetic resonance imaging sequence. This technique can elucidate significant information about the health and development of human tissue such as liver and brain, and has been used on phantom models (e.g., agar, silicone) to determine their suitability for use as a mechanical surrogate for human tissues in experimental models. The applied harmonic deformation used in MRE is generated by an actuator, transmitted in bursts of a specified duration, and synchronized with the magnetic resonance signal excitation. These actuators are most often a pneumatic design (common for human tissues or phantoms) or a piezoelectric design (common for small animal tissues or phantoms). Here, we describe how to design and assemble both a pneumatic and a piezoelectric MRE actuator for research purposes. For each of these actuator types, we discuss displacement requirements, end-effector options and challenges, electronics and electronic-driving requirements and considerations, and full MRE implementation. We also discuss how to choose the actuator type, size, and power based on the intended material and use. © 2022 Wiley Periodicals LLC.

Basic Protocol 1: Design, construction, and implementation of a convertible pneumatic MRE actuator for use with tissues and phantom models

Basic Protocol 2: Design, construction, and implementation of a piezoelectric MRE actuator for localized excitation in phantom models

Keywords: biomechanics \bullet magnetic resonance elastography \bullet MRE \bullet magnetic resonance imaging \bullet MRI

How to cite this article:

Triolo, E. R., Khegai, O., Ozkaya, E., Rossi, N., Alipour, A., Fleysher, L., Balchandani, P., & Kurt, M. (2022). Design, construction, and implementation of a magnetic resonance elastography actuator for research purposes. *Current Protocols*, 2, e379. doi: 10.1002/cpz1.379

INTRODUCTION

Historically, pathologies such as tumors or lesions have been identified by physicians by manually palpating soft tissue to compare the mechanical properties of healthy

Triolo et al.

1 of 26



¹Department of Mechanical Engineering, University of Washington, Seattle, Washington

²Icahn School of Medicine at Mount Sinai, Biomedical Engineering and Imaging Institute, New York, New York

³Department of Mechanical Engineering, Stevens Institute of Technology, Hoboken, New Jersey

⁴Corresponding author: mkurt@uw.edu

tissue to potentially malignant tissues. This technique is not feasible, however, for internal organs such as the brain, making it necessary to develop a secondary method of producing these results, or even more accurate results, such as magnetic resonance elastography (MRE) (Hirsch, Braun, & Sack, 2017; Muthupillai et al., 1996). Elastography is a technique for determining the mechanical response of a material using an applied deformation and a motion-sensitive imaging modality (Greenleaf et al., 1996). There are many different methods to apply the necessary force for tissue deformation, and magnetic resonance imaging (MRI) is a popular method of detection. In MRE, the most common approach for recurrently deforming tissue in a controlled manner is through harmonic vibration (Greenleaf et al., 2000). Viscoelastic models are used to extract structural information from MRE measurements by establishing a mathematical relationship between the harmonic vibration applied and the resulting tissue deformation (Kurt et al., 2019; Kwon et al., 2009; Manduca et al., 2002; Papazoglou, Hirsch, Braun, & Sack, 2012; Van Houten, Miga, Weaver, Kennedy, & Paulsen, 2001; Yin et al., 2007). Performing MRE on brain tissue can provide information on different brain structures (including cell density, myelination, inflammation, and functional activation) based on their mechanical properties (i.e., magnitude of the complex shear modulus, damping ratio) (Fehlner et al., 2014; Guo et al., 2013; Hiscox et al., 2018, 2020; Huston et al., 2015, 2016; Johnson et al., 2016; Kurt et al., 2019; McIlvain, Schwarb, Cohen, Telzer, & Johnson, 2018; Murphy et al., 2016; Pattison, Lollis, Perrinez, Weaver, & Paulsen, 2009; Perry et al., 2017; Sack et al., 2009, 2011; Streitberger et al., 2011; Zhang, Green, Sinkus, & Bilston, 2011). These mechanical parameters can then be used to diagnose pathologies such as multiple sclerosis, Alzheimer's disease, and Parkinson's disease, or to indicate disease progress (ElSheikh et al., 2017; Gerischer et al., 2016; Hiscox et al., 2019; Johnson et al., 2017; Lipp et al., 2013, 2018; Murphy et al., 2011, 2016; Streitberger et al., 2012; Wuerfel et al., 2010). Additionally, because the tissue is viscoelastic, its mechanical response is dependent on loading speed or, in the case of MRE, the frequency of actuation. Therefore, some studies use multifrequency MRE, in which the vibration is applied and encoded at different frequencies to determine viscoelasticity (Kurt et al., 2019; Lipp et al., 2013; Neumann et al., 2018; Ozkaya et al., 2021).

When performing MRE on any tissue type, harmonic vibration must be induced in the tissue in synchronization with the motion-encoding gradient (MEG) (Hirsch et al., 2017; Muthupillai et al., 1996). Because this process requires a type of harmonic actuator that can be used to actuate tissue inside an MRI machine, the actuator (or at least the part of the driver unit used inside the scanner room) must be MR compatible. In general, there are three main categories of actuators. The first type is an indirect actuator, which uses an active driver outside of the scanner room and a passive driver inside the scanner (Asbach et al., 2008; Chang et al., 2016; Chaze et al., 2019; Feng et al., 2018; Freimann et al., 2012; Gruwel, Latta, Matwiy, & Tomanek, 2010; Latta et al., 2011; Yin, Rouviere, Glaser, & Ehman, 2008). In this type of actuator, usually pneumatic, an active driver that generates vibration is placed in the control room as opposed to the scanner room, and a passive driver is placed inside the scanner in contact with the tissue of interest (Asbach et al., 2008; Chang et al., 2016; Chaze et al., 2019; Feng et al., 2018; Freimann et al., 2012; Gruwel et al., 2010; Latta et al., 2011; Yin et al., 2008). A long rod or tube is then used to transmit the vibration from the active driver to the passive driver (Asbach et al., 2008; Chang et al., 2016; Chaze et al., 2019; Feng et al., 2018; Freimann et al., 2012; Gruwel et al., 2010; Latta et al., 2011; Yin et al., 2008). The Resoundant (www.resoundant.com) is a commercial pneumatic MRE device of this type that is used to diagnose liver fibrosis without a tissue biopsy. To the best of our knowledge, it is the only commercially available MRE actuator and has been extensively tested in various studies across different organ systems (Tse et al., 2009; Venkatesh, Yin, & Ehman, 2013). The passive component of this device has also been altered in various studies investigating

the human brain and phantoms (Badachhape, Okamoto, Johnson, & Bayly, 2018; Chaze et al., 2019; Hiscox et al., 2018; Zheng et al., 2007). The advantages of using a pneumatic actuator are that they generally allow for precise control and have good MR compatibility of the passive driver (Latta et al., 2011), and custom-built versions are inexpensive and have a simple design. These are typically the designs used for brain MRE due to their versatility and ability to produce large enough actuation amplitude (Chaze et al., 2019; Freimann et al., 2012; Sack et al., 2009). However, these designs typically have phase lag and therefore difficulties in synchronization control due to the long transmission tubes or rods necessary to transmit vibration (Neumann et al., 2018).

A second category of actuator takes advantage of the static magnetic field by using an electromagnetic coil or coils to induce vibration. Current passing through an electromagnetic coil results in an oscillating magnetic field. Based on the Lorentz force law, if the surface normal vector of the coil is perpendicular to the static magnetic field of the MRI machine, a rotary motion is generated (Uffmann, Abicht, Quick, Ulbrich, & Ladd, 2001). This rotary motion is transferred to the tissue using some type of vibration pad or bite bar (for brain MRE) (Hamhaber, Grieshaber, Nagel, & Klose, 2003, 2010; Liu et al., 2009; Sack, Bernarding, & Braun, 2002; Suga et al., 2003; Uffmann et al., 2001). This type of design is inexpensive and can be manufactured using standard metal machining equipment (Tse et al., 2009). Additionally, a wide range of frequencies and displacements can be produced by changing the thickness of the wire, amount of current, or number and radius of coils (Uffmann et al., 2001). Nonetheless, this design is not commonly used anymore and its application is generally limited due to MRI safety challenges associated with its metallic structure. Two other main drawbacks are that the coil is mostly inflexible in terms of positioning and the induced magnetic field can potentially cause artifacts in the image (Tse et al., 2009).

The third category of actuator uses an active vibrational component that directly interfaces with the tissue, as opposed to the previous two categories where the active component is a distance away from the tissue and relies on a rod, pad, or pillow to transmit vibration over that distance. For this type of actuator, the entire unit must be MR compatible and small enough to attach to the tissue of interest. These units are usually driven by air pressure or piezoelectric crystals (Brauck, Galbán, Maderwald, Herrmann, & Ladd, 2007; Gordon-Wylie et al., 2018; Meinhold, Ozkaya, Ueda, & Kurt, 2019; Namani, Wood, Sakiyama, & Bayly, 2009; Neumann et al., 2018; Numano et al., 2013; Ozkaya et al., 2021; Rossman, Glaser, Felmlee, & Ehman, 2003; Runge et al., 2019; Uffmann, Abicht, Grote, Quick, & Ladd, 2002; Yin, Kearney, Magin, & Klatt, 2017). The main drawback of this type of device is that they are usually quite bulky and have difficulty attaching to the tissue (Tse et al., 2009). This type of actuator, particularly the piezoelectric type, is most commonly used for MRE of small animals or phantoms (Brauck et al., 2007; Meinhold et al., 2019; Namani et al., 2009; Ozkaya et al., 2021; Rossman et al., 2003; Uffmann et al., 2002; Yin et al., 2017).

There is currently a need for research-specific MRE actuators for various tissue types at multiple field strengths. Although there are device design papers that describe a specific custom pneumatic actuator (e.g., Feng et al., 2018; Latta et al., 2011) for research purposes, there is no paper that describes how to design, build, and implement an MRE actuator in general. In designing the MRE actuators used in our research lab, we encountered many questions and challenges regarding design and construction. Here, we endeavor to answer such questions and provide guidance for other laboratories attempting to design and implement their own MRE system for research studies in tissue or phantom mechanics. We also aim to offer validation methods and part selection guidelines for various MRE actuator applications. We describe how to design and assemble both a pneumatic actuator (see Basic Protocol 1) and a piezoelectric actuator (see Basic

Protocol 2) using all commercially available electronic components. For each of type, we discuss displacement requirements, end-effector options and challenges, electronics and electronic-driving requirements and considerations, and full MRE implementation. We also discuss how to choose the actuator type, size, and power based on the intended material and use.

BASIC PROTOCOL 1

DESIGN, CONSTRUCTION, AND IMPLEMENTATION OF A CONVERTIBLE PNEUMATIC MRE ACTUATOR FOR USE WITH TISSUES AND PHANTOM MODELS

This protocol describes a convertible pneumatic MRE actuator for research on multiple tissue types that uses all commercially available electronic components. The design is illustrated in Figure 1. This protocol can be utilized to develop an actuator for MRE of human brain, other human tissue, or a phantom. We specifically focus on construction of an end-effector for distributed vibration at the surface of a phantom or brain, but the design can be used for most tissue types. To use with a different tissue type, the design of the tissue-contacting end-effector can be altered. We also discuss how to select different components if the requirements for the actuator are different from those described here or if the components are not available in a particular location.

At the end of this protocol, the following should have been achieved: (1) the active components (subwoofer, amplifier, signal generator) have been selected based on the intended use; (2) the subwoofer has been modified and an end-effector shape has been chosen and manufactured; (3) *optional*: the vibration amplitude and frequency response of the end-effector have been verified using a laser Doppler vibrometer or other similar system; (4) the entire setup has been implemented in the MRI equipment and scanner rooms; and (5) a proof-of-concept scan has been performed on a phantom or human tissue, and wave-field images and an octahedral shear strain signal-to-noise ratio (OSS-SNR) have been generated to evaluate the vibration within the phantom or tissue.

Materials

NOTE: Components used in our configuration are listed in italics. They can be replaced with others that perform the same function, as described in the protocol.

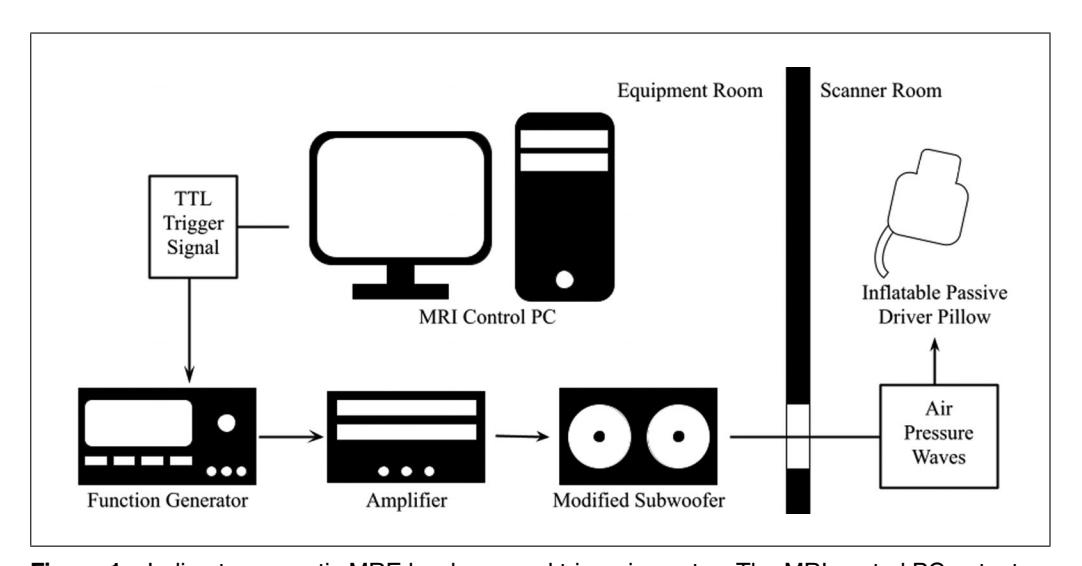


Figure 1 Indirect pneumatic MRE hardware and triggering setup. The MRI control PC outputs a TTL trigger signal during acquisition that drives a signal generator via external triggering. This, in turn, sends a predetermined signal through the amplifier to the subwoofer, which then pushes air pressure waves through rubber tubing into the tissue-contacting end-effector.

Active actuation components:

Rubber-coned subwoofer in an enclosure (MTX Audio Terminator Series TNE212D, 1200-W Dual 12-in. Sub Enclosure)

Class-D audio power amplifier (*Behringer Monitor Speaker and Subwoofer part NX3000*)

Signal generator (RIGOL DG1022 Series Dual-Channel Function/Arbitrary Waveform Generator)

Appropriate cabling for active components:

Banana-to-Speakon male speaker wire audio adapter

3-foot Eightwood 75- Ω BNC male–to–3.5-mm mono male coaxial power audio cable

10-foot MillSO headphone adapter TRS ½-in. male-to-3.5-mm female stereo jack

10-foot Monoprice 75- Ω BNC male connector BNC cable

Passive end-effector components:

3D printer (Anycubic i3 Mega)

Thermoplastic polyurethane (TPU) 3D printer filament (*Overture TPU filament*, 1.75 mm, 1 kg spool)

Polylactic acid (PLA) 3D printer filament (eSUN PLA PRO (PLA+) filament, 1.75 mm, 1 kg spool, gray)

Cyanoacrylate glue (BSI MAXI-CURE)

Stiff rubber tubing (firm clear polyurethane rubber tubing for drinking water, ³/₄-in. i.d., 1½,6 in. o.d., 25 ft. length, McMaster-Carr, cat. no. 5439K25)

Clear acrylic sheet (scratch- and UV-resistant cast acrylic, $48 \times 48 \times \frac{1}{8}$ in., McMaster-Carr)

CNC machine, laser cutter, or jigsaw and power drill

Hex key set or screwdriver set (depending on screws on subwoofer)

Hot glue gun and hot glue or caulking silicone

Clamps

MRI-compatible tape

MRI-compatible adhesive bandage

Component selection

- 1. Select an appropriate rubber-coned subwoofer and corresponding Class-D audio power amplifier based on the intended use.
 - a. Frequency response: The frequency response of the subwoofer and amplifier should be in an appropriate range for the human tissue being imaged, generally:
 - 45-80 Hz for heart (Arani et al., 2017; Barnhill et al., 2017; Rump, Klatt, Braun, Warmuth, & Sack, 2007; Wassenaar et al., 2016)
 - 40-70 Hz for kidney or liver (Asbach et al., 2010; Dittmann et al., 2017; Etchell, Jugé, Hatt, Sinkus, & Bilston, 2017; Feng et al., 2018; Lee et al., 2012; Marticorena Garcia et al., 2018; Morisaka et al., 2017; Sack, Jöhrens, Würfel, & Braun, 2013)
 - 30-150 Hz for skeletal muscle (Barnhill et al., 2013; Bensamoun et al., 2006; Hollis et al., 2016; Kennedy et al., 2020; Papazoglou, Rump, Braun, & Sack, 2006; Sack et al., 2002, 2013; Suga et al., 2001)
 - 40-60 for pancreas (Dittmann et al., 2017; Shi, Glaser, Venkatesh, Ben-Abraham, & Ehman, 2015, 2018)
 - 65-300 Hz for breast (Hawley et al., 2017; Plewes, Bishop, Samani, & Sciarretta, 2000; Van Houten, Doyley, Kennedy, Weaver, & Paulsen, 2003)
 - 25-100 Hz for brain (Guo et al., 2013; Hamhaber et al., 2010; Hiscox et al., 2020; Johnson et al., 2016; Kurt et al., 2019; Ozkaya et al., 2021; Xu, Lin, Xi, Shen, & Gao, 2007; Zhang et al., 2011)

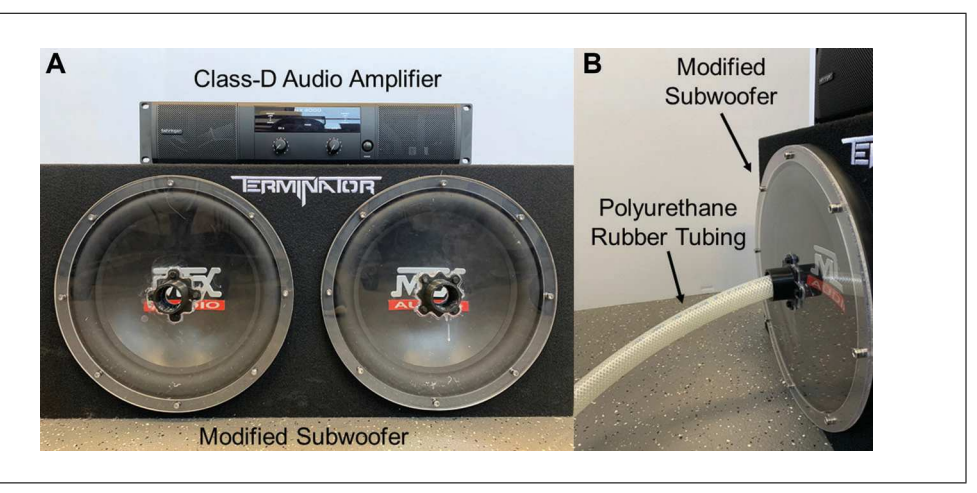


Figure 2 Full active actuation component setup. The components shown are kept in the equipment room of the MRI scanner. (A) Class-D audio amplifier (top) and 12-in. dual rubber cone subwoofer modified with acrylic disks over the cones to maintain air pressure. (B) Polyurethane rubber tubing connected to the front of a modified cone is used to push air pressure waves to the passive end-effector.

b. Power output: The maximum power output of the audio amplifier should be greater than the maximum power handling of the subwoofer at the impedance of the subwoofer for obtaining the maximum amplitude the subwoofer is capable of outputting.

Power and impedance considerations: The impedance of the subwoofer should be noted to ensure that the correct specifications are considered for the amplifier. Audio equipment typically has an impedance of 2 or 4 Ω . Most subwoofer specifications list one or the other, but technical specifications of amplifiers will list both, as they can usually amplify at either impedance.

Example: To perform MRE of human brain and a phantom, we selected a dual 12-in. sealed enclosure with a 1200 W maximum power handling at 2 Ω impedance (bottom component in Fig. 2A, modified in Fig. 2B) and a two-channel Class-D power amplifier with 1500 W maximum deliverable power per channel at 2 Ω impedance (top component in Fig. 2A).

Amplitude selection considerations: In our configuration, while both cones are driven simultaneously, only one 12-in. cone supplies air to the passive driver components. This amplitude is more than sufficient to apply vibration to a phantom material (less than half power selected on the amplifier) and is sufficient to apply vibration to the human brain (two thirds to maximum power selected on the amplifier).

For any speaker, the maximum volume of air that a cone can move (its peak diaphragm displacement volume) can be calculated by multiplying twice the maximum linear excursion (Xmax) by the surface area of the cone (Sd). These two values can usually be found in the data sheet for the speaker or can be requested from the manufacturer. This would be a good starting point for determining cone size and subsequently the amplifier power; however, there will be some loss between the cone and end-effector due to dampening. The movement of the end-effector can be determined using a laser Doppler vibrometer or an equivalent test (see Understanding Results), which would give the most accurate calculation of the amplitude supplied by the actuator.

- 2. Select a signal generator capable of being triggered by an external time-to-live (TTL) signal to output a specified signal burst.
- 3. Select the appropriate cabling to connect the input of the subwoofer to the output of the amplifier, the input of the amplifier to the output of the signal generator, and the external TTL triggering input of the signal generator to the TTL trigger output of the MRI scanner.

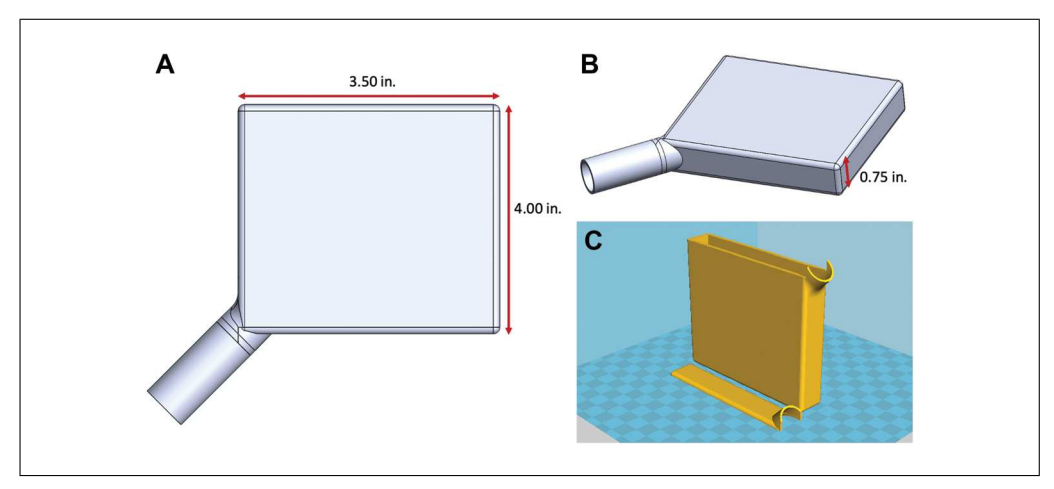


Figure 3 Design of flat end-effector design. (**A,B**) Top and isometric views of 3D CAD model showing assembled components of a flat end-effector. (**C**) How the components are 3D printed to keep the end-effector hollow.

Audio cabling is not standardized, so the cabling required is dependent on the components selected in steps 1-2. In our case, the TTL output of the MRI scanner and TTL triggering input of the signal generator require a BNC male—to—BNC male cable, but this may differ for other systems.

Example: In our configuration, we utilized a male dual banana—to—male Speakon cable to connect the subwoofer to the amplifier, a ¼-in. male—to—3.5-mm female and 3.5-mm male—to—BNC male cable to connect the amplifier to the signal generator, and a BNC male—to—BNC male cable to connect the signal generator to the MRI scanner output.

4. Select firm, flexible tubing to connect the active components (selected in steps 1-3) to the tissue-contacting passive component.

The tubing must be long enough to reach from the active components in the MRI equipment room, through the waveguide, and into the MRI scanner bore. It should be flexible enough to make all necessary turns without necessitating connectors, but firm enough to not absorb and therefore dampen vibration along its length.

Example: In our configuration, we used 25 ft of clear polyurethane rubber tubing with ³/₄-in. inner diameter, 3.5-in. bend radius, and 85A durometer.

Building and manufacturing

5. Using CAD software, design a hollow end-effector based on the intended use.

For a phantom, the end-effector should be relatively the same size as the phantom surface.

For brain tissue, the end-effector should mimic the shape of the MRI scanner head coil for patient comfort.

For other tissue, the end-effector should be re-sized based on the tissue and easily connectable to the tissue.

Design considerations: Creating a hollow end-effector may require printing in multiple parts (see examples in Figs. 3 and 4). Depending on the shape and thickness of the end-effector, internal supports may be needed to prevent complete compression of the end-effector by the tissue. This is particularly important for an end-effector contacting the human head, as the full weight of the head presses on a particularly thin pillow (Fig. 4). To overcome this, we insert the 3D printer supports used to print the cap portion of the end-effector into the center of the pillow before it is fully sealed (Fig. 5).

Example: In our configuration, we 3D print the end-effector in two main components, with multiple 3D-printed custom tubing segments. We attach these components with cyanoacrylate glue and seal the seams with hot glue to maintain air pressure and add strength to the potentially vulnerable joints. This process is shown in Figure 5.

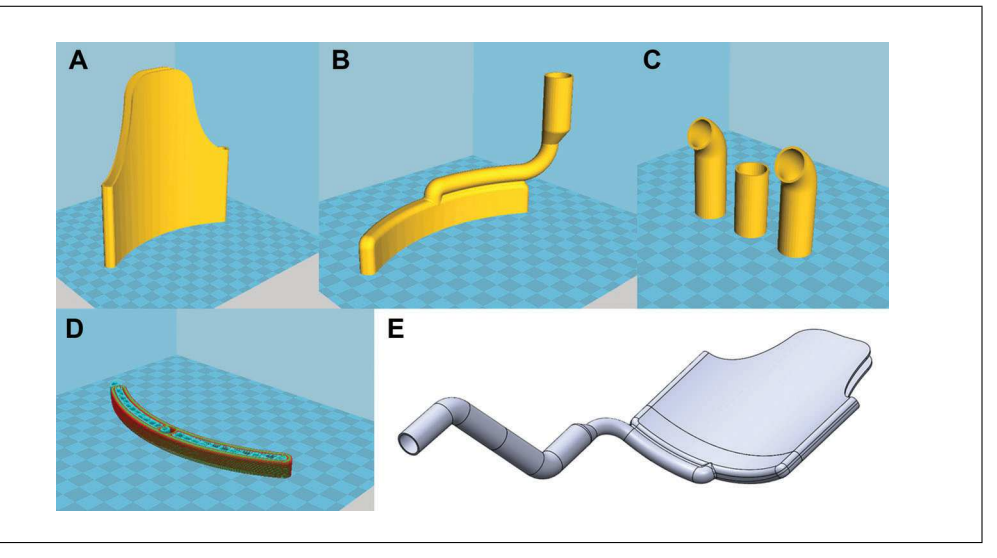


Figure 4 Design of human brain end-effector. The main body (**A**), end cap (**B**), and tubing bends (**C**) are 3D printed separately to create an end-effector that remains hollow. Supports (**D**) are used to print the end cap and then pulled out once the print has been completed. Assembly (**E**) of components A-C forms the full pillow.

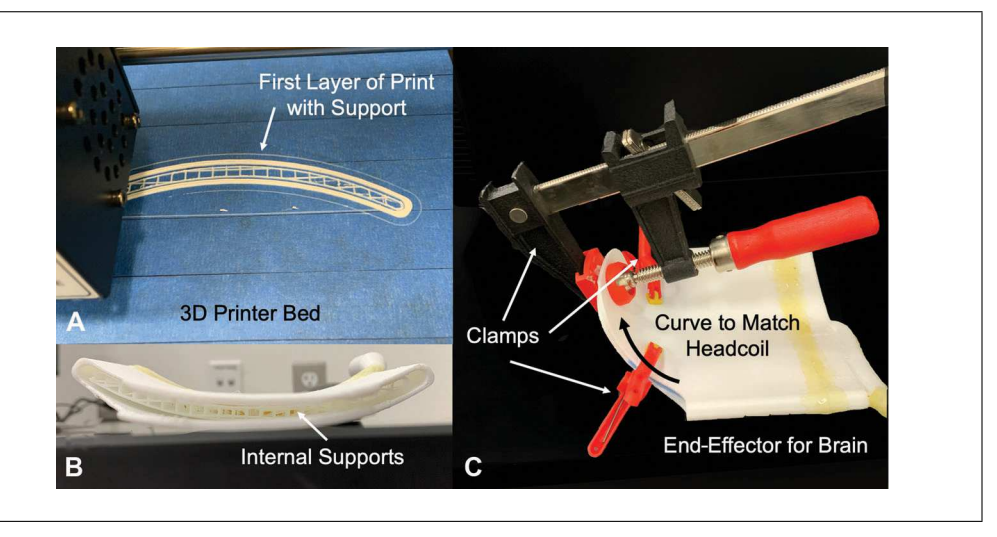


Figure 5 Construction of human brain end-effector. As the end-cap prints, supports (**A**) are printed along with it to support the top of the cap during printing. After the supports are removed, they are placed inside the main body of the pillow (**B**) to prevent the weight of the head from fully compressing the pillow. (**C**) The separate components are glued together, and the top of the pillow is clamped and glued in a curved shape to match the shape of the head coil.

- 6. Print the parts of the custom end-effector on a 3D printer using TPU filament. Assemble the pieces using cyanoacrylate glue, hot glue, and/or silicone and clamp together until the glue/silicone is set (Fig. 5C).
- 7. Using a CNC machine, laser cutter, or jigsaw and power drill, cut the acrylic sheet to match the shape and size of the front of the subwoofer, with a small hole in the center approximately the size of the selected tubing (Fig. 6A,C). Also include holes at the edge as needed to attach the piece of acrylic to the front of the subwoofer cone (Fig. 6A,C). Use the existing screws (used to hold the subwoofer cone in its enclosure) to attach the piece of acrylic to the front of the cone.

This is used to channel air through the tubing (also see Fig. 2B) and maintain air pressure.

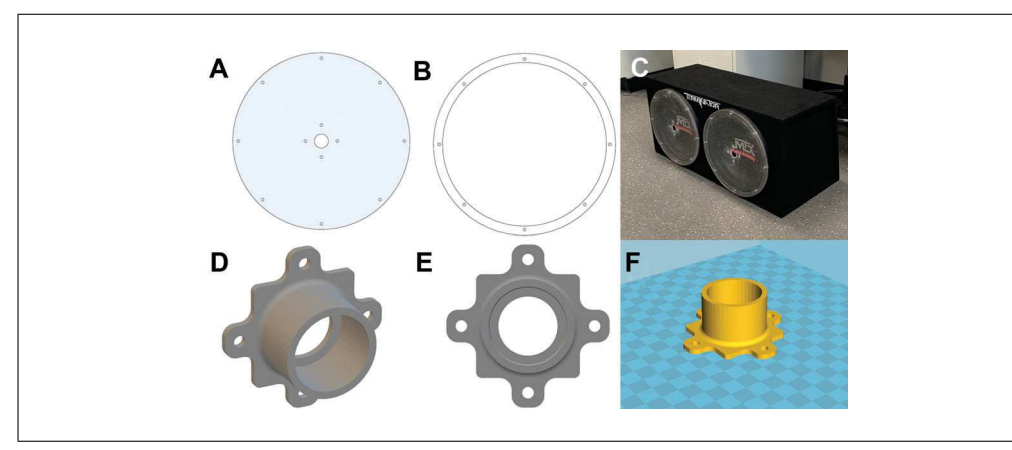


Figure 6 Modification of the subwoofer with acrylic disk and 3D-printed tubing connector. (**A,B**) CAD models of acrylic disk and ring. (**C**) Acrylic disks mounted to the front of subwoofer cones. (**D,E**) CAD models showing isometric and front views of tubing connector. (**F**) 3D printing of tubing connector.

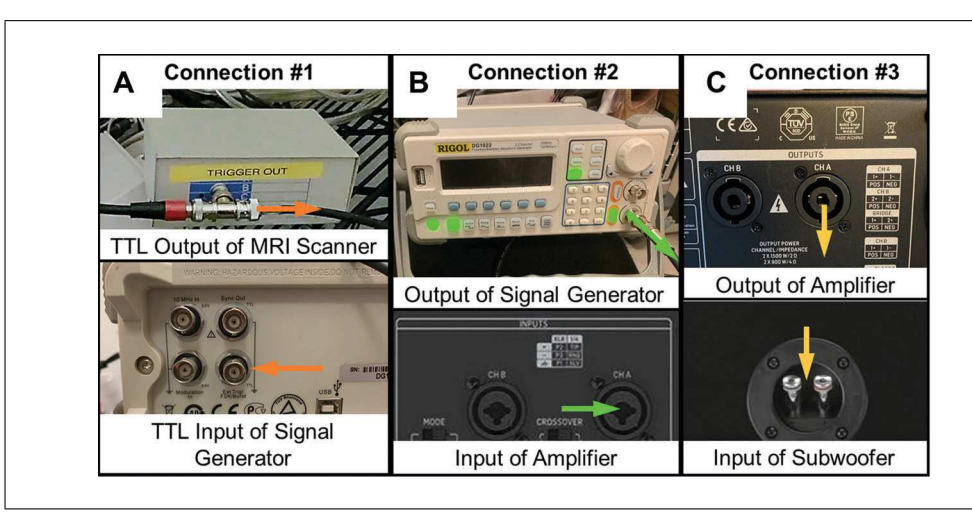


Figure 7 Cable connections. (**A**) A male-male BNC cable is used to connect the TTL output of the MRI scanner to the TTL external triggering input of the signal generator. (**B**) A BNC male—to—3.5-mm male cable and a 3.5-mm female—to—1/4-in. male adapter are used to connect the output of the signal generator to the input of the Class-D amplifier. (**C**) A Speakon male—to—banana male cable is used to connect the output of the amplifier to the input of the subwoofer.

Some rubber subwoofer cones have a raised portion next to the outside edge of the cone. In our configuration, we address this by cutting an acrylic ring (Fig. 6B) and attaching it underneath the acrylic disk. This raises the disk enough that it won't compress the raised part of the cone.

8. Use CAD software to design a custom connector for attaching the tubing to the acrylic sheet (Fig. 6D-F). 3D print the connector using PLA filament, attach it to the sheet (before or after attaching the sheet to the speaker cone) using cyanoacrylate glue and/or 3D-printed pegs/screws, and seal the edges with hot glue.

Implementation and testing

9. Place all active components (i.e., modified subwoofer, audio amplifier, signal generator, and associated cabling) in the MRI scanner equipment room. Use the appropriate cabling to connect the TTL trigger output of the scanner to the TTL external triggering port on the signal generator, the output of the signal generator to the "audio in" on the audio amplifier, and the "subwoofer out" on the audio amplifier to the input on the modified subwoofer (Fig. 7).

The trigger output is standard with the scanners used (3T Skyra and 7T Terra, Siemens Healthineers) and is the same for any other application that requires triggering. Some scanners (e.g., Siemens) use a fiber optic output that can be altered to any cable type using a media converter. Other scanners (e.g., Phillips) have a direct BNC TTL output. The signal itself is programmed in the pulse sequence (timing and duration of TTL signal) with Siemens IDEA pulse programming environment.

10. Connect one end of the flexible tubing to the custom 3D-printed connector on the modified subwoofer before feeding the other end of the tubing through the waveguide into the MRI scanner room. Next, attach the custom end-effector to the end of the tubing that is now inside the scanner room using MRI-compatible tape.

Using MRI-compatible tape instead of glue makes it more convenient to switch out the end-effector so the same actuator can be used to apply vibration to a variety of tissues or phantoms. If a more permanent connection is desired, using glue before moving the tubing and end-effector into the MRI scanner room is a viable option.

11. Turn on the signal generator, set the desired vibration frequency, and set the peak-to-peak voltage amplitude (*V*p-p) to 1 V with no voltage or phase offset.

To test the vibration output and select the appropriate amplitude, turn on the output from the signal generator without external triggering and adjust the volume (use the knob) on the audio amplifier to adjust the amplitude. Leave the knob at the desired amplitude and turn off the signal generator's output.

Vibration amplitude is adjusted using the volume knob on the audio amplifier as opposed to changing the input voltage on the signal generator. Most audio equipment has a maximum input voltage of 1 Vp-p with no voltage offset, so these settings should not be adjusted.

Some signal generators are more programmable or have more functionalities than others. There is not enough information sent from the MRI scanner to the signal generator inherently to cause any of these changes, but changes in frequency and/or cycles after a certain amount of time or cycles can be programed into some signal generators. For the signal generator described here, this option does not exist, and frequencies and cycles need to be changed manually.

Alternatively, a microcontroller could be used as an intermediary between the trigger sent from the scanner and the signal generator to augment the signal generator's capabilities. The signal generator could then be set either manually from a remote location (i.e., the MRI control room) or automatically based on the output from the scanner should the sequence output a different trigger signal dependent on the frequency specified. In this case, the sequence can be programmed such that multiple or specific triggering signal trains are sent depending on the frequency used in the sequence, and the signal generator or microcontroller can be programmed to output the corresponding frequency.

12. Set up the external triggering and cycle output on the signal generator. Use the burst option on the signal generator to select external triggering as the source for an *N*-cycles output and select the appropriate number of cycles (*n*). Again, turn on the output of the signal generator; the vibration should only begin when triggered by the MRI sequence.

The number of cycles is dependent on the repetition time (TR) selected and vibration frequency, or rather TR must be adjusted to the integer number of cycles (n) multiplied by the vibration period (1/f) such that the burst of vibration stops at the end of the TR and begins again at the start of the next TR. Therefore, if the TR is set, the TR can be multiplied by the frequency to calculate the integer number of cycles needed for that acquisition. Because there is a minimum TR necessary to require one slice, there is a minimum n to be used as the number of cycles selected on the signal generator. See Figure 8 for a representation of TR and frequency shown on the MRE sequence diagram.

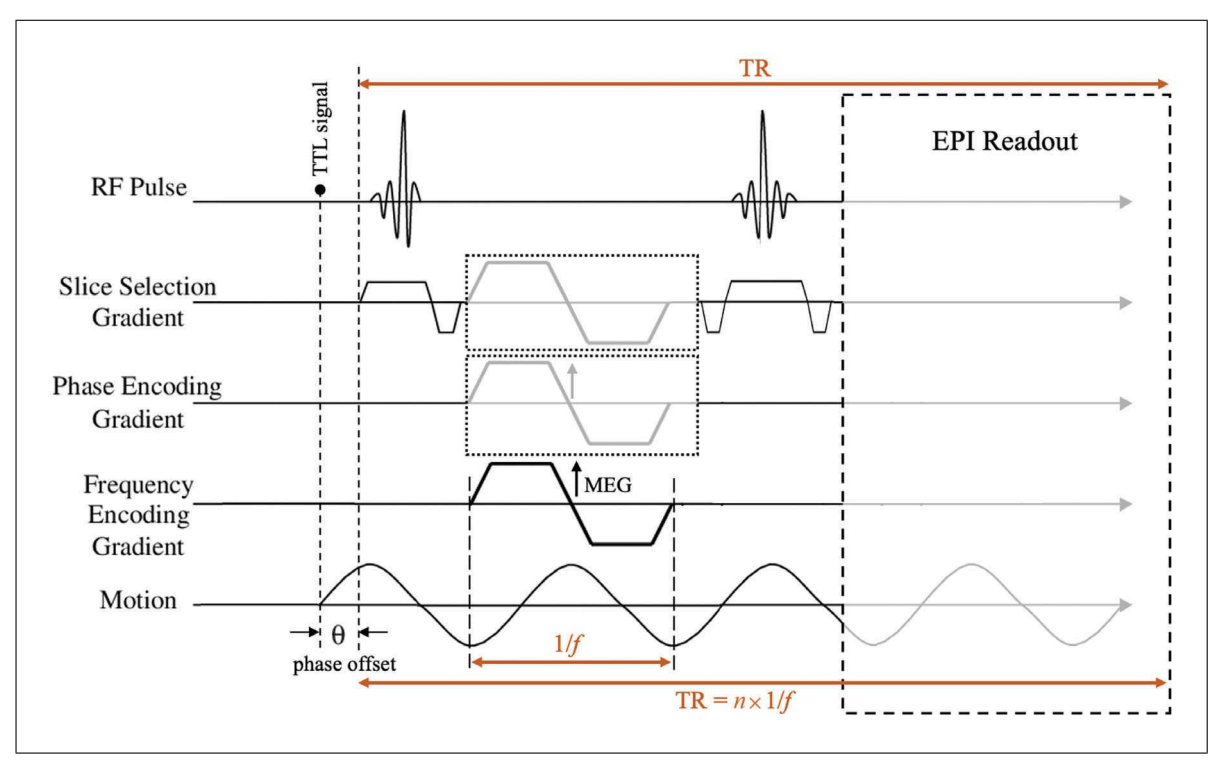


Figure 8 Labeled sequence diagram. A 2D EPI multi-slice MRE sequence with 3D motion encoding gradients is shown and labeled with the trigger (TTL) signal, phase offset (θ) , vibration period (1/f), and true repetition time (TR).

- 13. Place the end-effector in the appropriate position for the tissue or phantom and begin the MRE scan protocol.
 - a. For human brain, place the end-effector under the head as if it were a pillow. The end-effector will remain in place due to the weight of the head.
 - b. For other human tissue, place the end-effector on the tissue of interest and attach with an MRI-safe adhesive bandage so it is pressed firmly against the tissue without causing pain or discomfort.
 - c. For a phantom, place the end-effector on the surface of the phantom and attach it using an MRI-safe strap adhesive bandage so it does not move from the intended position during scanning.
- 14. For the first proof-of-concept scan of the subject of interest, test multiple vibration amplitudes and select the amplitude that is best for both patient comfort and usefulness in post-processing (Fig. 9).

If the vibration amplitude is too low, shear waves are not generated sufficiently for viscoelastic inversion analysis, resulting in a low signal-to-noise ratio. If the vibration amplitude is too high, it will be uncomfortable for the patient and cause excessive shear wave reflection, resulting in an inaccurate wavelength-based stiffness estimate and low OSS-SNR (McGarry et al., 2011) in areas surrounding internal boundaries.

Prior to the proof-of-concept scan, the vibration amplitude and frequency response of the weighted and/or unweighted end-effector can be measured using laser Doppler vibrometry to determine suitability. After the proof-of-concept scans, wavefield images and the OSS-SNR should be evaluated to quantitatively observe vibration quality in the tissue. The OSS-SNR should be relatively uniform throughout the tissue; any asymmetry is likely indicative of a scanning artifact, lack of vibration amplitude in one part of the tissue, or internal wave reflection due to a vibration amplitude that is too high. Alternatively, a lack of amplitude in one part of the tissue will be concurrent with a lack of amplitude in the wavefield image. For more details regarding quantitative troubleshooting, see Understanding Results.

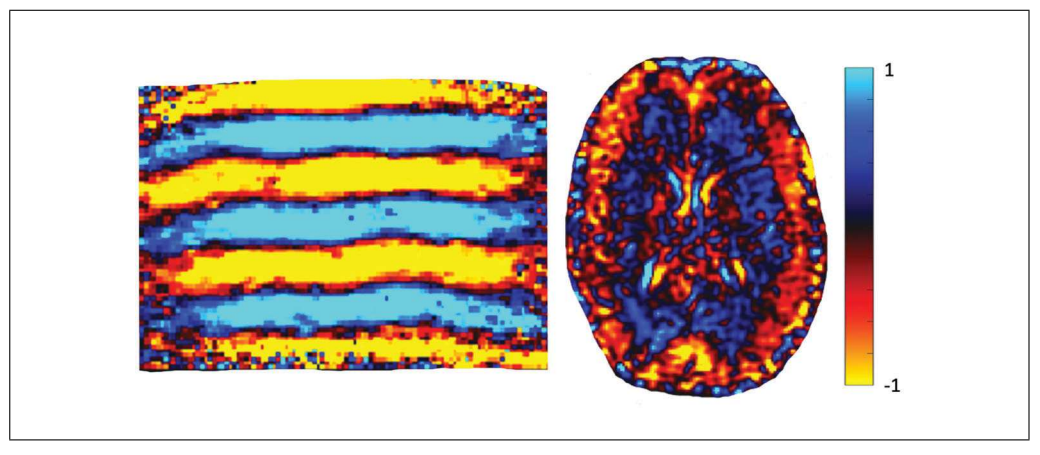


Figure 9 Wavefield images of a phantom (left) and human brain (right) captured utilizing a 7T MRE sequence and the actuator described in Basic Protocol 1.

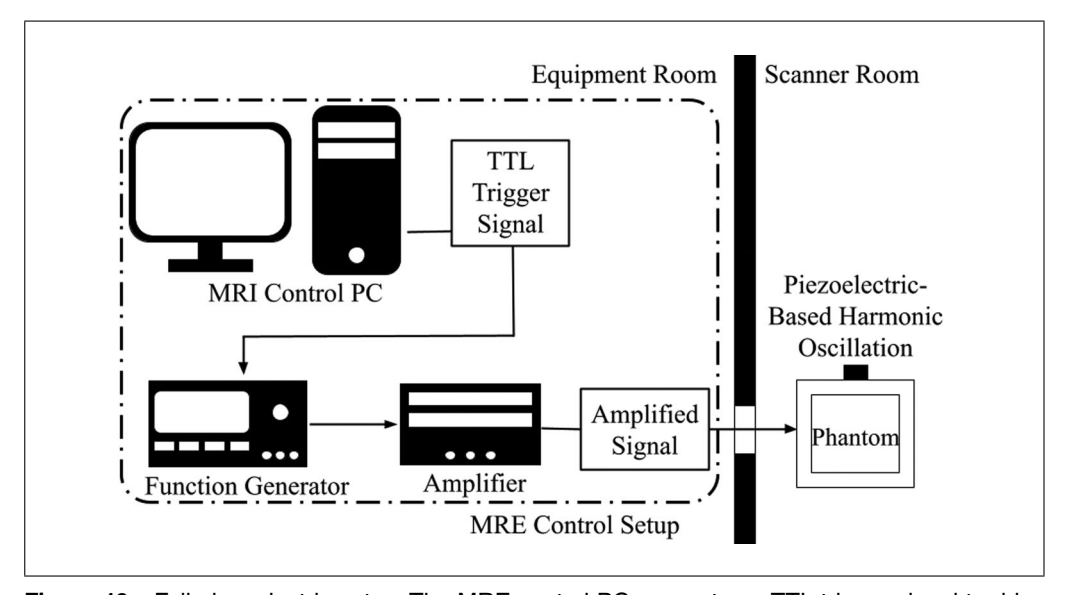


Figure 10 Full piezoelectric setup. The MRE control PC generates a TTL trigger signal to drive the piezoelectric actuator through the amplifier and the function generator via the external trigger input port.

BASIC PROTOCOL 2

DESIGN, CONSTRUCTION, AND IMPLEMENTATION OF A PIEZOELECTRIC MRE ACTUATOR FOR LOCALIZED EXCITATION IN PHANTOM MODELS

While the actuator designed in Basic Protocol 1 can be used on a tissue or phantom to apply distributed harmonic deformation across the entire surface, this actuator design is for phantom MRE only and is specifically to apply localized harmonic deformation. This protocol is useful because some phantom materials are not conducive to surface harmonic deformation due to their size or surface texture. Additionally, localized deformation is preferred over distributed deformation when investigating wave propagation in all three directions as opposed to determining material stiffness, and for investigations involving multiple material types and/or boundaries. This setup is illustrated in Figure 10. As for Basic Protocol 1, it uses all commercially available electronic components.

At the end of this protocol, the following should have been achieved: (1) the active components (piezoelectric actuator, amplifier, signal generator) have been selected based on the intended use; (2) an end-effector shape has been chosen and manufactured, and the phantom holder has been designed and manufactured; (3) *optional:* the vibration amplitude and frequency response of the piezoelectric actuator have been verified using a laser

Doppler vibrometer or other similar system; (4) the entire setup has been implemented in the MRI equipment and scanner rooms, and a phantom material has been chosen; and (5) a proof-of-concept scan has been performed on the phantom, and wavefield images and an OSS-SNR have been generated to evaluate the vibration within the phantom.

Materials

NOTE: Components used in our configuration are listed in italics. They can be replaced with others that perform the same function, as described in the protocol.

Active actuation components:

MRI-compatible piezoelectric actuator (Cedrat Technologies APA150NM)

Linear amplifier for piezo (*Cedrat Technologies LA75C*)

Signal generator (RIGOL DG1022 Series Dual-Channel Function/Arbitrary Waveform Generator)

Appropriate cabling for active components (two 10-foot Monoprice 75- Ω BNC male connector BNC cables)

Passive holder/attachment components:

3D printer (Anycubic i3 Mega)

Polylactic acid (PLA) 3D printer filament (eSUN PLA PRO (PLA+), 1.75 mm, 1 kg spool, gray)

MRI-compatible phantom holder material and double-sided tape (depending on desired design)

Phantom material (e.g., silicone, agar)

Philips-head screwdriver (depending on piezoelectric actuator)

CNC machine, laser cutter, or jigsaw and power drill

Phantom holder example design (square, to fit 16-channel Siemens Healthineers headcoil)

Clear cast acrylic sheet $(24 \times 24 \times \frac{1}{2})$ -in. and $12 \times 12 \times \frac{1}{8}$ in., McMaster-Carr, cat. nos. 8560K268 and 8560K239)

Double-sided tape (10-foot \times ½-in. heavy-duty acrylic strong-adhesive removable double-sided mounting tape, clear)

Nylon screws (metric pan-head Phillips screws, 3M, 12-mm length, McMaster-Carr, cat. no. 92492A719)

Soft foam

Hot glue gun and hot glue or calking silicone

Component selection

- Select an MRI-compatible piezoelectric actuator and corresponding linear amplifier
 (a Cedrat actuator and amplifier are shown in Fig. 11). The frequency response of the
 actuator and amplifier should be in the appropriate range for the intended use, generally 30-200 Hz. The manufacturer of the piezoelectric actuator should recommend
 a compatible linear amplifier.
- 2. Select a signal generator capable of being triggered by an external TTL signal to output a specified signal burst.
- 3. Select the appropriate cabling to connect the input of the actuator to the output of the amplifier, the input of the amplifier to the output of the signal generator, and the external triggering input of the signal generator to the TTL trigger output of the MRI scanner. Ensure that the cable connecting the actuator to the amplifier is long enough to reach from the MRI equipment room, through the waveguide, and into the MRI scanner bore.

The appropriate cabling to connect the actuator to the amplifier should be included with the purchase of the device. We used BNC male-to-BNC male cables to connect the amplifier input to the signal generator output and to connect the TTL triggering input of the

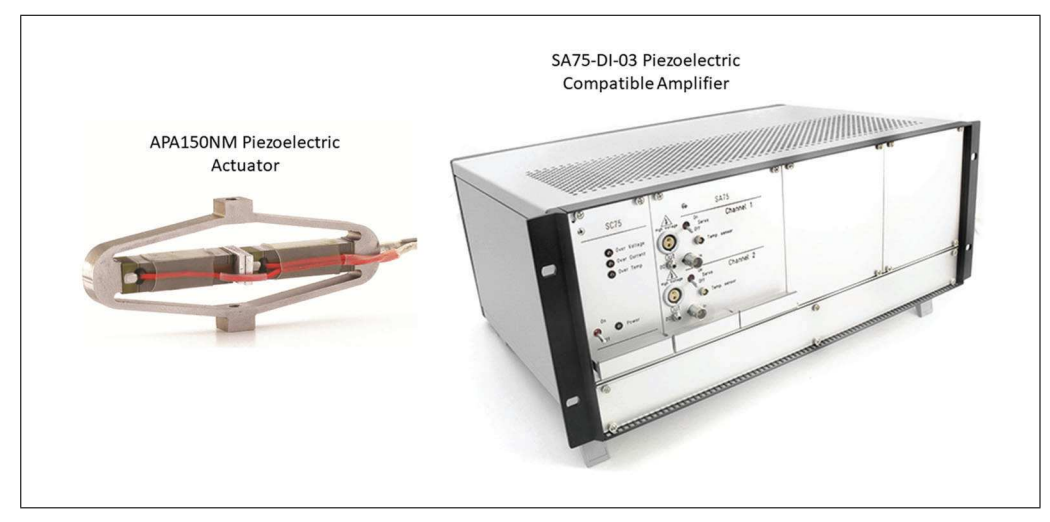


Figure 11 Cedrat Technologies piezoelectric actuator and amplifier. The APA150NM piezoelectric actuator is MRI-safe (NM standing for nonmagnetic). The compatible amplifier (SA75-DI-03) it is connected to is kept in the equipment room.

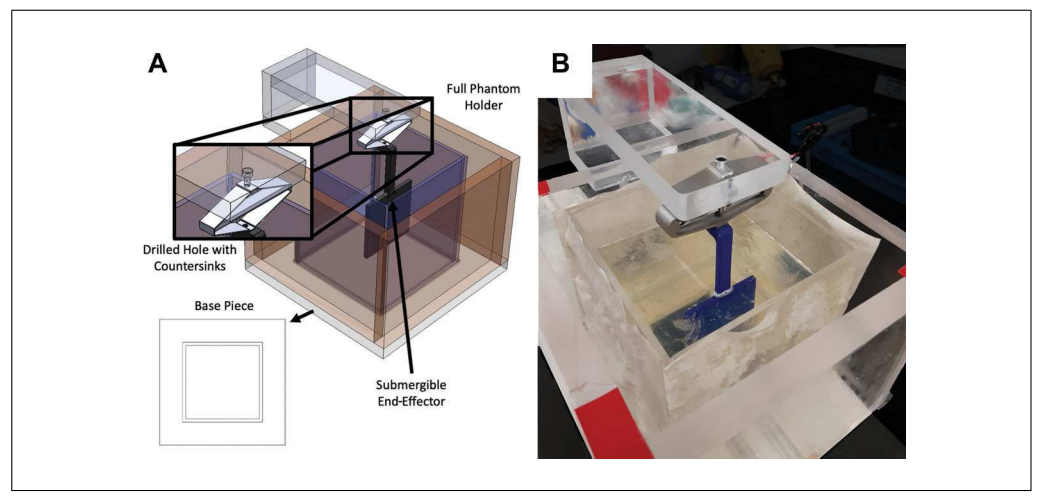


Figure 12 Example phantom holder design. (**A**) CAD model of fully constructed phantom holder showing the location of the ½-in.-thick outer walls (orange), base (white), actuator holder parts (gray) with drilled hole, piezoelectric actuator (silver), and ½-in.-thick inner walls (purple) to contain the phantom. The submergible end-effector (black) is screwed to the end of the actuator using a nylon screw, and the liquid phantom material is poured around it into the purple-walled container. Black lines show an enlargement of the actuator and screws. (**B**) Phantom holder with phantom material cured around the end-effector (blue).

signal generator to the TTL output of the MRI scanner. The latter will be dependent on the MRI scanner setup.

4. Select MRI-compatible materials and construct a non-metallic phantom holder to both contain the phantom and hold the actuator in the intended position, ensuring that it fits inside the MRI coil.

An example is shown in Figure 12, but any phantom shape required can be manufactured.

Building and manufacturing

- 5. Manufacture and build the phantom holder designed in the previous step.
 - a. Use a CNC machine, laser cutter, jigsaw, or other equivalent machine to cut pieces of ½-in.-thick acrylic sheet with the following dimensions:

one each at 6×6 in., 4.4×2 in., 2×2 in., and 2×1.25 in. four at 4×5 in.

- b. In the center of the 6×6 -in. piece, cut a 3.75×3.75 -in. square slit that is 0.1 in. deep and 0.14 in. wide.
 - This is the base of the box in which the phantom will cure (white in Fig. 12A).
- c. Cut four pieces of $\frac{1}{8}$ -in.-thick acrylic sheet with dimensions of 4.1×3.875 in.
- d. Place the four 1/8-in.-thick pieces in the square slit of the base and secure with hot glue or calking silicone. Ensure that there are no air holes in the seams by pouring water into the completed box and checking for leaks.
 - This completes the box in which the phantom will cure (purple in Fig. 12A).
- e. Line up the four 4×5 –in. pieces on the outer edges of the base and secure with double-sided tape.
 - These are the outer walls of the holder (orange in Fig. 12A).
- f. Drill a 0.1-in.-diameter hole through the 4.4×2 -in. piece so it is in the center of the short dimension and a ½ in. from one end in the long dimension.
 - This is the screw hole for securing the actuator to the holder (gray in Fig. 12A).
- g. Drill two countersinks centered on opposite sides of the 0.1-in. hole: one as a 0.6-cm-deep, 0.6-cm-diameter circle and the other as a 0.5×0.9 -cm rectangle.
 - These provide seats for the nylon screw and the top of the actuator (gray in Fig. 12A).
- h. Attach the 4.4×2 -in., 2×2 -in., and 2×1.25 -in. pieces together and then to the outer wall of the holder using double-stick tape as shown in Figure 12A, with the screw hole facing the center of the holder and the rectangular countersink facing towards the base.
- i. Place foam between the inner and outer walls to dampen vibration.
- 6. Use CAD software to design a vibration end-effector to be submerged into the phantom on one end and connected (via a nylon screw) to the actuator on the other side. 3D print the end-effector using PLA+ filament.
 - An example of an end-effector in place is shown in Figure 12.
- 7. Use a nylon screw to attach the actuator to the phantom holder, using the countersinks to ensure that it is fully secure. Use another nylon screw to attach the endeffector to the actuator such that the end-effector extends into the area in which the phantom material will be poured (Fig. 12A).
- 8. Mix the liquid phantom material as desired and pour into the phantom holder such that the end-effector is partially submerged and allow the phantom to cure around the end-effector (Fig. 12B).
 - Good coupling between the end-effector and phantom material is required for shear wave transmission, so it is important for the end-effector to be submerged in the phantom material and for the phantom to cure around the end-effector as opposed to inserting or pressing the end-effector into the surface of a cured phantom.

Implementation and testing

- 9. Once the phantom has fully cured, place the phantom holder and attached piezoelectric actuator into the MRI coil and run the actuator cable away from the phantom and through the waveguide into the MRI equipment room.
- 10. Place the amplifier for the actuator and the signal generator into the MRI equipment room. Attach the cables from the actuator to the appropriate amplifier output, and attach the amplifier input to the signal generator output.

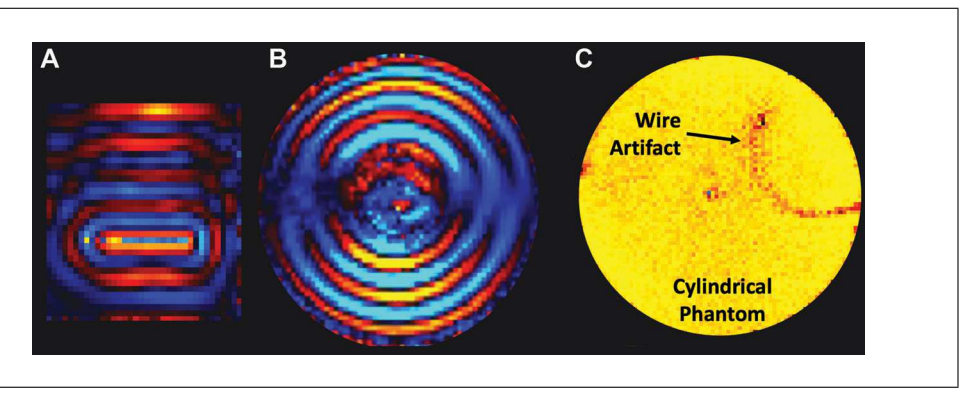


Figure 13 Wavefield images obtained utilizing the piezoelectric actuator setup described in Basic Protocol 2 of (**A**) a phantom in the configuration described and (**B**) a phantom in an alternate cylindrical configuration. (**C**) The cable from the piezoelectric actuator was resting too close to a cylindrical phantom and caused interference in the shape of the cable.

- 11. Use the appropriate cabling to connect the TTL trigger output of the scanner to the TTL external triggering port on the signal generator.
- 12. Turn on the signal generator, set the desired vibration frequency, and set the *V*p-p amplitude to 5 V with a 2.5-V DC offset and no phase offset.

To test the vibration output and select the appropriate amplitude, turn on the output from the signal generator without external triggering.

The voltages and operation of the amplifier/actuator setup should be based on the information provided in the data sheet for the selected components.

13. Set up the external triggering and cycle output on the signal generator. Use the burst option on the signal generator to select external triggering as the source for an *N*-cycles output and select the appropriate number of cycles (*n*). Again, turn on the output of the signal generator; the vibration should only begin when triggered by the MRI sequence (Fig. 13).

The number of cycles is dependent on the TR selected and the vibration frequency. Multiply the TR by the frequency to calculate the integer number of cycles needed for that acquisition. See Figure 8 for a representation of TR and frequency shown on the MRE sequence diagram.

Prior to the proof-of-concept scan, the stroke length and frequency response of the weighted and/or unweighted piezoelectric actuator can be measured using laser Doppler vibrometry to determine suitability. After the proof-of-concept scans, wavefield images and the OSS-SNR should be evaluated to quantitatively observe vibration quality in the phantom material. The OSS-SNR should be uniform throughout the phantom; any asymmetry is likely indicative of a scanning artifact, lack of vibration amplitude in one part of the phantom, or internal wave reflection due to a vibration amplitude that is too high. Alternatively, a lack of amplitude in one part of the phantom will be concurrent with a lack of amplitude in the wavefield image. For more details regarding quantitative troubleshooting, see Understanding Results.

COMMENTARY

Background Information

MRE is a technique for determining the mechanical response of soft materials using applied harmonic deformation of the material and a motion-sensitive MRI sequence. Use of this technique on human tissue (e.g., liver, brain) can provide significant information

about its health and development. The applied harmonic deformation is generated by an actuator, transmitted in bursts of a specified duration, and synchronized with the MR signal excitation. Because this harmonic vibration must be induced in the tissue in synchronization with the motion encoding

gradient (Hirsch et al., 2017; Muthupillai et al., 1996), this process requires a type of harmonic actuator that can be used inside an MRI machine. Therefore, the actuator—or at least the part of the driver unit used inside the scanner room—must be MR compatible. The actuator must also be able to provide a wide range of vibration amplitudes and frequencies, as different tissue types require different parameters (see Basic Protocol 1, step 1). The frequency range (bandwidth) of the actuator should match the frequency range necessary for the tissue of interest. Additionally, because biological tissues exhibit viscoelastic behavior, the mechanical response of tissue is dependent on loading speed or, in the case of MRE, the frequency of actuation. Therefore, some studies use multifrequency MRE, in which the vibration is applied and encoded at different frequencies to determine viscoelasticity (Kurt et al., 2019; Lipp et al., 2013; Neumann et al., 2018; Ozkaya et al., 2021).

As described in detail in the Introduction, there are three main categories of MRE actuator. First, there are indirect actuators (usually pneumatic) that use an active driver outside of the scanner room and a passive driver inside the scanner. Second, an electromagnetic coil or coils can be used to induce vibration by using the static magnetic field by using current to induce rotary motion according to the Lorentz force law. This rotary motion is transferred to the tissue using some type of vibration pad or bite bar (for brain MRE). Third, the actuator can apply the vibration directly to the tissue of interest, where a small, fully MR-compatible actuation unit, usually driven by air pressure or piezoelectric crystals, is attached. Each actuator type has its own benefits and drawbacks.

Currently, there is a need for researchspecific MRE actuators for various tissue types at multiple field strengths. Here, we describe how to design and assemble both a pneumatic actuator and a piezoelectric actuator using all commercially available electronic components for research purposes. In Basic Protocol 1, we discuss how to design, construct, and implement a convertible pneumatic actuator. This protocol can be utilized to develop an actuator for MRE of the human brain, other human tissue, or phantom. In Basic Protocol 2, we discuss how to design, construct, and implement a piezoelectric actuator for use only on phantoms. While piezoelectric actuators have also historically been used to study MRE in small animals, our piezoelectric protocol is described only for use in phantoms. The electrical component setup could be used in small animal MRE, but designing a holder for both the animal and the actuator would require significant modification of the building and manufacturing described. The actuator in Basic Protocol 1 can be used on a phantom to apply distributed harmonic deformation across the entire surface, whereas the one in Basic Protocol 2 is used specifically to apply localized harmonic deformation.

Critical Parameters

Actuator active components

The subwoofer and corresponding power amplifier must be selected based on the intended use, as their frequency responses should be in an appropriate range for the tissue being imaged. Additionally, the subwoofer should have rubber cones as opposed to fabric cones in order to maintain air pressure between the cone and acrylic sheet. For power considerations, audio equipment typically has an impedance of 2 or 4 Ω . Most subwoofer specifications list one or the other, whereas amplifier specifications will list both because amplifiers can usually perform at either impedance. The impedance of the subwoofer needs to be considered to ensure that the correct specifications are being considered for the amplifier. Additionally, the maximum power output of the audio amplifier should be greater than the maximum power handling of the subwoofer at the impedance of the subwoofer to obtain the maximum amplitude the subwoofer is capable of outputting. Generally, the TTL output of the MRI scanner and TTL triggering input of the signal generator require a BNC male-to-BNC male cable, but the cabling required will depend on the components selected because audio cabling is not standardized. The output of the signal generator should be 1 Vp-p maximum with no voltage offset, as this is the maximum allowable input that will not cause damage to most audio equipment. Vibration amplitude should be adjusted using the volume knob on the amplifier rather than changing the input voltage on the signal generator.

Piezoelectric actuator

The commercial piezoelectric actuator and the cabling required to connect it to the amplifier must be MRI-safe, and this may require approval from an MRI safety committee or other administrative body. The phantom holder must be able to fit inside the coil being used during scanning. A 16-channel head coil was used in our scans due to its ability to

acquire with a high signal-to-noise ratio, but this does impose a size restriction on both the phantom and the phantom holder. The voltage and voltage offset values, rather than being one set number as in audio equipment, are determined by the manufacturer. This information is likely in the device datasheet, but can also be acquired from the manufacturer's technical services or after-sales department. Proper operation (including voltage and frequency settings) is essential for preventing damage to the equipment, so the actuator should be driven only within the frequency and voltage ranges that the actuator and cabling are rated for. The frequency range (bandwidth) of the piezoelectric actuator should therefore match the requirements for the intended study. Additionally, because of the power in the cabling, it is recommended that the cable be kept as far from the phantom as possible to avoid artifacts that obscure the captured wavefield image (Fig. 13C).

General vibration

If the vibration amplitude is too low, sufficient shear waves for viscoelastic inversion analysis will not be generated and there will be a low signal-to-noise ratio. If the vibration amplitude is too high, it will be uncomfortable for the patient (in human scans) and cause excessive shear wave reflection, resulting in an inaccurate wavelength-based stiffness estimate and low OSS-SNR in areas surrounding internal boundaries. After the first set of proof-of-concept scans, the calculation of both wavefield images and OSS-SNR can be used to determine if the vibration amplitude is appropriate. A lack of amplitude in one part of the tissue will be concurrent with a lack of amplitude in the wavefield image, so calculating and observing the wavefield, especially in a uniform phantom, is an important step in determining if the vibration amplitude is at an appropriate level. A secondary method to determine if the vibration amplitude is appropriate and directed in the correct direction is to calculate OSS-SNR. The OSS-SNR should be uniform within the phantom, and asymmetry is likely indicative of a scanning artifact, lack of vibration amplitude in one part of the tissue, or internal wave reflection due to an excessively high vibration amplitude. (For more information on both of these parameters, see Understanding Results.) Therefore, multiple amplitudes should be tested before determining the final scanning protocol for a particular study. The external triggering of the signal generator should be run on an N-cycles burst setting. The number of cycles per burst to run the signal generator is dependent on the TR selected and vibration frequency. The TR is multiplied by the frequency to calculate the integer number of cycles needed for that acquisition. Finally, the coupling between the end-effector and the tissue or phantom is crucial to vibration transfer. For the pneumatic actuator, the end-effector pillow should be firmly pressed against the surface of the tissue or phantom, whether it is held down by body weight (under the subject) or secured tightly with an MRI-safe adhesive bandage. For the piezoelectric actuator, the phantom should cure around the end-effector to ensure full adhesion.

Troubleshooting

Human brain end-effector challenges

For our specific application on the human brain, we implemented multiple iterations of end-effector design based on multiple technology development scans on healthy human volunteers. Multiple pillow designs were manufactured and tested for effective and even vibration application and patient comfort, resulting in a final design that (1) matches the shape of the head coil (for 7T MRI scanners) without any sharp ridges and (2) is thin enough to allow scans in a diverse patient population (Fig. 14). The size and shape are dependent on the head coil, and similar design issues will arise for other multichannel head coils. Our initial pillow design did not provide sufficient vibration, whereas our second design provided enough vibration but was not comfortable for the duration of the scan. Similarly, our third pillow design provided sufficient vibration, but was not fully comfortable due to a ridge in the back, and was too thick to allow us to scan a diverse patient population. Our fourth design did not initially provide sufficient vibration due to pillow compression under the weight of the head. Adding soft supports to the inside of the pillow where the head rests made the pillow comfortable and still provided sufficient vibration. Due to concerns about uneven application of vibration, we made modified the inlet to make it central to the pillow, resulting in our final design.

Subwoofer does not output sound/ piezoelectric actuator does not vibrate

General

The first step for troubleshooting this problem is to ensure that every component is plugged in, powered on, and has the correct settings, and that the signal generator is set

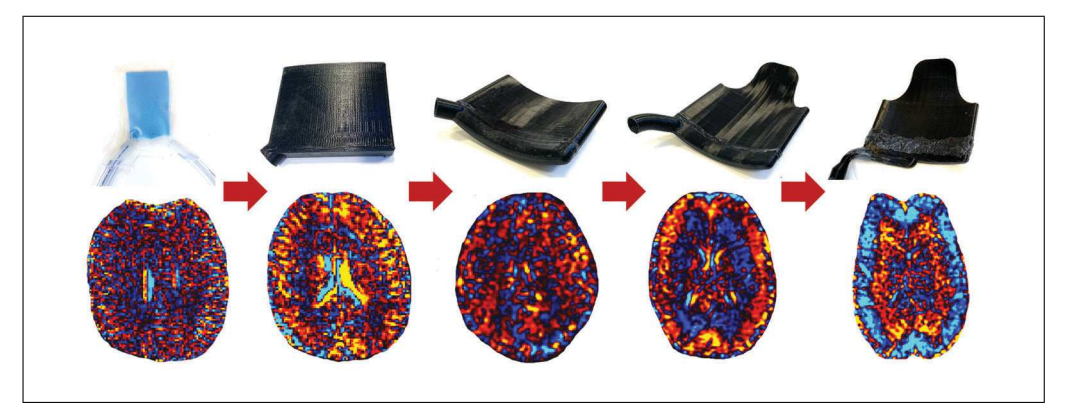


Figure 14 Evolution of the pneumatic MRE human brain end-effector (earliest to latest from left to right) with corresponding wavefield images.

to output a consistent signal with no external triggering. The next step is to ensure that all cable connections are snug and to utilize a multimeter to check that all cables are working properly. If any cables are loose or not working, they should be replaced before attempting to run the device again. If this is not the issue, a multimeter or oscilloscope should be used to ensure that the signal generator is outputting the expected signal. If it is not, the signal generator should be replaced. If that is not the problem, a multimeter or oscilloscope should be used to ensure that the amplifier is outputting an amplified signal as expected. If not, the amplifier should be repaired or replaced. If none of these steps have revealed the issue, the problem is likely the subwoofer (in Basic Protocol 1) or piezoelectric actuator (in Basic Protocol 2).

During scans

If the subwoofer is outputting or the piezoelectric actuator is vibrating when the signal generator is set to output a consistent signal with no external triggering, it is first important to check cable connections. The external triggering port in the equipment room should be connected via a cable to the MRI scanner. To ensure that a trigger signal is being output, the scanner's external triggering port (in the equipment room) should be connected to an oscilloscope and the MRE sequence run to observe outputs. If there is no trigger signal output, it may need to be enabled within the sequence, or the cable connections may be incorrect or a cable may be broken. The cables should be tested to see if this is the case. If the trigger signal is being output, the external triggering port on the signal generator should be checked to be sure it is correct, or a new signal generator should be used if this does not solve the problem.

Subwoofer stops outputting sound above a certain volume

This problem can occur when the amplifier overvolts, and it is important to immediately turn the amplifier down and off to avoid damage to the equipment. If this occurs consistently at a 1 Vp-p input to the amplifier, it is likely because the maximum power output of the amplifier is not greater than the maximum power handling of the subwoofer at the impedance of the subwoofer. A simple option is to mark on the amplifier knob the level at which this occurs and not turn the knob past that mark. Another option is to reduce the input voltage. Finally, the recommended option for obtaining the maximum amplitude the subwoofer is capable of outputting is to replace the power amplifier with a more powerful one.

Excessive damping from subwoofer cone to end-effector

Excessive dampening can occur due to tubing connections or the softness of the tubing used. If the tubing is too soft, it can directly dampen the air pressure waves, in which case it should be replaced with stiffer tubing. Any tube splitter or connector will also cause dampening, as the air pressure wave will reflect and cause destructive interference; it is recommended that one continuous piece of tubing (with no connectors) be used to connect the subwoofer cone to a single-inlet end-effector.

Understanding Results

It is imperative to determine that the actuator is operating at the correct frequency and with sufficient amplitude before use in the intended tissue. One method for determining this is to use, as an example, a laser Doppler vibrometer to achieve an accurate estimate of the unloaded actuator frequency and its frequency response (Curtis, Zhang, Khalilzad-Sharghi,

Boulet, & Othman, 2012; Ozkaya et al., 2021; Triolo et al., 2021). This method can also be used to determine the time delay from signal generator output to end-effector vibration in the case of the pneumatic actuator (Triolo et al., 2021). This time delay can also be calculated based on the speed of sound in the length of tubing, but empirical measurement is far more accurate in this case. Once it is confirmed that the actuator is producing vibration at the expected amplitude and frequency, the next step is to determine if the actuator is coupled with the tissue or phantom well enough to produce shear waves with sufficient SNR in the collected phase images. When looking at a wavefield image in a homogeneous material (a phantom, typically used for validation) the shear wave should be clearly visible with the expected wavelength and propagation speed based on stiffness-based estimates and as shown in Figures 9 and 13. Should the wavefield look over-saturated (where the phase is wrapped multiple times for one wave peak), the vibration amplitude should be decreased. Should the expected wavelength be barely visible, the amplitude should be increased. This is difficult to determine in human tissue, however, as in the brain shown in Figure 9.

One way to determine if the vibration amplitude is appropriate and directed in the correct direction is to calculate the OSS-SNR (McGarry et al., 2011). The OSS-SNR should be uniform within the tissue of interest, and any asymmetry is likely indicative of a scanning artifact, lack of vibration amplitude in one part of the tissue, or internal wave reflection. Generally, an average OSS-SNR of 3 or above is considered acceptable (McGarry et al., 2011). This will also be reflected in the stiffness reconstruction of the tissue or phantom. A lack of amplitude in one part of the tissue will be concurrent with a lack of amplitude in the wavefield image. To fix asymmetry due to lack of amplitude in one part of the tissue, the end-effector should be repositioned or the amplitude increased to increase the penetration of the traveling wave. Internal wave reflection, usually due to boundaries and/or shear wave interactions, can be caused by application of an amplitude that is too high. This will cause not only asymmetry in OSS-SNR and stiffness reconstruction maps, but also visible oversaturation in the wavefield images. In this case, the amplitude should be decreased.

Overall, the purpose of MRE is to determine the mechanical properties of tissues or other materials. Performing MRE on a tissue can provide information on different struc-

tures within that tissue based on their mechanical properties (i.e., magnitude of the complex shear modulus, damping ratio) using a viscoelastic inversion (e.g., local frequency estimation, algebraic inversion, or nonlinear inversion) calculation on the captured wavefield images (Honarvar, Sahebjavaher, Rohling, & Salcudean, 2017; Maharjan et al., 2020; Van Houten et al., 2001). In the brain, these properties can provide information on cell density, myelination, inflammation, and functional activation (Fehlner et al., 2014; Guo et al., 2013; Hiscox et al., 2018, 2020; Huston et al., 2015, 2016; Johnson et al., 2016; Kurt et al., 2019; McIlvain et al., 2018; Murphy et al., 2016; Pattison et al., 2009; Perry et al., 2017; Sack et al., 2009, 2011; Streitberger et al., 2011; Zhang et al., 2011). These mechanical parameters can then be used to diagnose pathologies such as multiple sclerosis, Alzheimer's disease, and Parkinson's disease, or to indicate disease progress (ElSheikh et al., 2017; Gerischer et al., 2016; Hiscox et al., 2019; Johnson et al., 2017; Lipp et al., 2013, 2018; Murphy et al., 2011, 2016; Streitberger et al., 2012; Wuerfel et al., 2010). As stated earlier, MRE is used by pathologists to diagnose liver fibrosis, and may also be applicable to other diagnostic applications such as breast cancer, prostate cancer, and pancreatic masses (Arani, Eskandari, Ouyang, & Chopra, 2017; Doyley, Weaver, Van Houten, Kennedy, & Paulsen, 2003; Glaser, Felmlee, & Ehman, 2006; Shah et al., 2004; Shi et al., 2018; www.resoundant.com).

Time Considerations

Lead times on components can range from one day for smaller materials to several weeks for complex electronic components such as the piezoelectric actuator and amplifier, audio amplifier, subwoofer, and signal generator. These major components should be ordered well in advance of the planned experiments, as smaller components (e.g., cabling, screws) that correspond to a specific major component will likely need to be ordered after the major components arrive. Manufacturing the endeffector (by 3D printing, gluing, clamping) will take 3 hr for the piezoelectric end-effector and one day for the pneumatic human brain end-effector.

Cost Considerations

For the pneumatic actuator, the most costly components are the signal generator, audio amplifier, and subwoofer. Used/refurbished signal generators with the required functionality range from about \$150 to \$400, and

new ones can cost upwards of \$1000. The cost of the audio amplifier will range widely based on power, with low-wattage amplifiers costing under \$100 and high-wattage ones costing over \$500. The 3000-W dual-channel amplifier in Figure 2 costs around \$300, and an amplifier from the same brand with twice the power costs around \$500. The subwoofer cost ranges based on size and quality, generally from \$50 to \$250. The one in Figure 2 costs about \$170. The cost of 3D printing. machining, and assembly is dependent on the materials, personnel, and equipment available. For the piezoelectric actuator, the cost of the actuator itself was around \$2000 and the cost of a used/refurbished amplifier was \$400. A new amplifier would cost \$1000 to \$2000. The same signal generator as mentioned for the pneumatic actuator was used here. Various phantom materials of varying costs can be used with this protocol, but the least costly would be Knox unflavored gelatin at around \$15 per pound. Again, the cost of 3D printing, machining, and assembly is dependent on the materials, personnel, and equipment available.

Acknowledgments

The authors would like to acknowledge funding from NSF awards 1953323 and 1826270.

Author Contributions

E. R. Triolo: Conceptualization, investigation, methodology, writing (original draft, reviewing, and editing); O. Khegai: Investigation, methodology, writing (reviewing and editing); E. Ozkaya: Conceptualization, investigation, methodology, writing (reviewing and editing); N. Rossi: Investigation, methodology; A. Alipour: Methodology, supervision, writing (reviewing and editing); P. Balchandani: Funding acquisition, supervision, writing (reviewing and editing); M. Kurt: Conceptualization, funding acquisition, project administration, supervision, writing (reviewing and editing).

Conflict of Interest

The authors declare no conflict of interest.

Data Availability Statement

All final CAD models referenced in this article are available for download as Supplementary Information.

Literature Cited

Arani, A., Eskandari, A., Ouyang, P., & Chopra, R. (2017). A novel high amplitude piezoceramic

- actuator for applications in magnetic resonance elastography: A compliant mechanical amplifier approach. *Smart Materials and Structures*, 26(8), 1–10. doi: 10.1088/1361-665×/aa71f2.
- Arani, A., Glaser, K. L., Arunachalam, S. P., Rossman, P. J., Lake, D. S., Trzasko, J. D., ... Araoz, P. A. (2017). In vivo, high-frequency three-dimensional cardiac MR elastography: Feasibility in normal volunteers. *Magnetic Resonance in Medicine*, 77(1), 351–360. doi: 10.1002/mrm. 26101.
- Asbach, P., Klatt, D., Hamhaber, U., Braun, J., Somasundaram, R., Hamm, B., & Sack, I. (2008).
 Assessment of liver viscoelasticity using multifrequency MR elastography. *Magnetic Resonance in Medicine*, 60(2), 373–379. doi: 10.1002/mrm.21636.
- Asbach, P., Klatt, D., Schlosser, B., Biermer, M., Muche, M., Rieger, A., ... Sack, I. (2010). Viscoelasticity-based staging of hepatic fibrosis with multifrequency MR elastography. *Radiology*, 257(1), 80–86. doi: 10.1148/radiol. 10092489.
- Badachhape, A. A., Okamoto, R. J., Johnson, C. L., & Bayly, P. V. (2018). Relationships between scalp, brain, and skull motion estimated using magnetic resonance elastography. *Journal of Biomechanics*, 73, 40–49. doi: 10.1016/j.jbiomech.2018.03.028.
- Barnhill, E., Hollis, L., Sack, I., Braun, J., Hoskins, P. R., Pankaj, P., ... Roberts, N. (2017). Nonlinear multiscale regularisation in MR elastography: Towards fine feature mapping. *Medical Image Analysis*, 35, 133–145. doi: 10.1016/j. media.2016.05.012.
- Barnhill, E., Kennedy, P., Hammer, S., Van Beek, E. J. R., Brown, C., & Roberts, N. (2013). Statistical mapping of the effect of knee extension on thigh muscle viscoelastic properties using magnetic resonance elastography. *Physiological Measurement*, *34*(12), 1675–1698. doi: 10.1088/0967-3334/34/12/1675.
- Bensamoun, S. F., Ringleb, S. I., Littrell, L., Chen, Q., Brennan, M., Ehman, R. L., & An, K. N. (2006). Determination of thigh muscle stiffness using magnetic resonance elastography. *Journal of Magnetic Resonance Imaging*, 23(2), 242–247. doi: 10.1002/jmri.20487.
- Brauck, K., Galbán, C. J., Maderwald, S., Herrmann, B. L., & Ladd, M. E. (2007). Changes in calf muscle elasticity in hypogonadal males before and after testosterone substitution as monitored by magnetic resonance elastography. *European Journal of Endocrinology*, 156(6), 673–678. doi: 10.1530/EJE-06-0694.
- Chang, W., Lee, J. M., Yoon, J. H., Han, J. K., Choi, B. I., Yoon, J. H., ... Suh, K. S. (2016). Liver fibrosis staging with MR elastography: Comparison of diagnostic performance between patients with chronic hepatitis B and those with other etiologic causes. *Radiology*, 280(1), 88–97. doi: 10.1148/radiol.2016150397.
- Chaze, C. A., McIlvain, G., Smith, D. R., Villermaux, G. M., Delgorio, P. L., Wright, H. G., ... Johnson, C. L. (2019). Altered brain tissue viscoelasticity in pediatric cerebral palsy measured

- by magnetic resonance elastography. *NeuroImage: Clinical*, 22, 101750. doi: 10.1016/j.nicl. 2019.101750.
- Curtis, E. T., Zhang, S., Khalilzad-Sharghi, V., Boulet, T., & Othman, S. F. (2012). Magnetic resonance elastography methodology for the evaluation of tissue engineered construct growth. *Journal of Visualized Experiments*, 60, 1–6. doi: 10.3791/3618.
- Dittmann, F., Tzschätzsch, H., Hirsch, S., Barnhill, E., Braun, J., Sack, I., & Guo, J. (2017). Tomoelastography of the abdomen: Tissue mechanical properties of the liver, spleen, kidney, and pancreas from single MR elastography scans at different hydration states. *Magnetic Resonance in Medicine*, 78(3), 976–983. doi: 10.1002/mrm. 26484.
- Doyley, M. M., Weaver, J. B., Van Houten, E. E. W., Kennedy, F. E., & Paulsen, K. D. (2003). Thresholds for detecting and characterizing focal lesions using steady-state MR elastography. *Medical Physics*, 30(4), 495–504. doi: 10.1118/1.1556607.
- ElSheikh, M. M., Arani, A., Perry, A., Boeve, B. F., Meyer, F. B., Savica, R., ... Huston, J. (2017). MR elastography demonstrates unique regional brain stiffness patterns in dementias. *American Journal of Roentgenology*, 209(2), 403–408. doi: 10.2214/AJR.16.17455.MR.
- Etchell, E., Jugé, L., Hatt, A., Sinkus, R., & Bilston, L. E. (2017). Liver stiffness values are lower in pediatric subjects than in adults and increase with age: A multifrequency MR elastography study. *Radiology*, 283(1), 222–230. doi: 10.1148/radiol.2016160252.
- Fehlner, A., Guo, J., Streitberger, K. J., Hirsch, S., Braun, J., & Sack, I. (2014). The viscoelastic response of the human brain to functional activation detected by magnetic resonance elastography. *Proceedings of the 22nd Annual Meeting of ISMRM, Milan, 2014*. Concord, CA: International Society of Magnetic Resonance in Medicine.
- Feng, Y., Zhu, M., Qiu, S., Shen, P., Ma, S., Zhao, X., ... Guo, L. (2018). A multi-purpose electromagnetic actuator for magnetic resonance elastography. *Magnetic Resonance Imaging*, 51, 29– 34. doi: 10.1016/j.mri.2018.04.008.
- Freimann, F. B., Streitberger, K. J., Klatt, D., Lin, K., McLaughlin, J., Braun, J., ... Sack, I. (2012). Alteration of brain viscoelasticity after shunt treatment in normal pressure hydrocephalus. *Neuroradiology*, 54(3), 189–196. doi: 10.1007/s00234-011-0871-1.
- Gerischer, L. M., Fehlner, A., Köbe, T., Braun, J., Sack, I., & Agnes, F. (2016). High resolution MR elastography of the hippocampus as a novel biomarker for Alzheimer's disease? *Clinical Neurophysiology*, 127(FV 12), e216–e217. doi: 10.1016/j.clinph.2016.05.029.
- Glaser, K. J., Felmlee, J. P., & Ehman, R. L. (2006). Rapid MR elastography using selective excitations. *Magnetic Resonance in Medicine*, *55*(6), 1381–1389. doi: 10.1002/mrm.20913.

- Gordon-Wylie, S. W., Solamen, L. M., McGarry, M. D. J., Zeng, W., VanHouten, E., Gilbert, G., ... Paulsen, K. D. (2018). MR elastography at 1 Hz of gelatin phantoms using 3D or 4D acquisition. *Journal of Magnetic Resonance*, 296, 112–120. doi: 10.1016/j.jmr.2018.08.012.
- Greenleaf, J. F., Muthupillai, R., Rossman, P. J., Lomas, D. J., Riederer, S. J., & Ehman, R. L. (2000). Measurement of tissue elasticity using magnetic resonance elastography. Review of Progress in Quantitative Nondestructive Evaluation, 16, 19–26.
- Greenleaf, J. F., Muthupillai, R., Rossman, P. J., Smith, J., Manduca, A., & Ehman, R. L. (1996). Direct visualization of strain waves by magnetic resonance elastography (MRE). *IEEE Ultrasonics Symposium*, 1, 467–472. New York: Institute of Electrical and Electronics Engineers.
- Gruwel, M. L. H., Latta, P., Matwiy, B., & Tomanek, B. (2010). Characterization of food stuffs using magnetic resonance elastography. Food Research International, 43(8), 2087–2092. doi: 10.1016/j.foodres.2010.07.015.
- Guo, J., Hirsch, S., Fehlner, A., Papazoglou, S., Scheel, M., Braun, J., & Sack, I. (2013). Towards an elastographic atlas of brain anatomy. *PLoS ONE*, 8(8), e71807. doi: 10.1371/journal. pone.0071807.
- Hamhaber, U., Grieshaber, F. A., Nagel, J. H., & Klose, U. (2003). Comparison of quantitative shear wave MR-elastography with mechanical compression tests. *Magnetic Resonance* in *Medicine*, 49(1), 71–77. doi: 10.1002/mrm. 10343.
- Hamhaber, U., Klatt, D., Papazoglou, S., Hollmann, M., Stadler, J., Sack, I., ... Braun, J. (2010). In vivo magnetic resonance elastography of human brain at 7 T and 1.5 T. Journal of Magnetic Resonance Imaging, 32(3), 577–583. doi: 10.1002/jmri.22294.
- Hawley, J. R., Kalra, P., Mo, X., Raterman, B., Yee, L. D., & Kolipaka, A. (2017). Quantification of breast stiffness using MR elastography at 3 tesla with a soft sternal driver: A reproducibility study. *Journal of Magnetic Resonance Imaging*, 45(5), 1379–1384. doi: 10.1002/jmri.25511.
- Hirsch, S., Braun, J., & Sack, I. (2017). Magnetic resonance elastography: Physical background and medical applications. Weinheim, Germany: Wiley-VCH.
- Hiscox, L. V., Johnson, C. L., McGarry, M. D. J., Marshall, H., Ritchie, C. W., van Beek, E. J. R., ... Starr, J. M. (2019). Mechanical property alterations across the cerebral cortex due to Alzheimer's disease. *Brain Communications*, 2(1), fcz049. doi: 10.1093/braincomms/fcz049.
- Hiscox, L. V., Johnson, C. L., McGarry, M. D. J., Perrins, M., Littlejohn, A., van Beek, E. J. R., ... Starr, J. M. (2018). High-resolution magnetic resonance elastography reveals differences in subcortical gray matter viscoelasticity between young and healthy older adults. *Neurobiology of Aging*, 65, 158–167. doi: 10.1016/j. neurobiolaging.2018.01.010.

- Hiscox, L. V., McGarry, M. D. J., Schwarb, H., Van Houten, E. E. W., Pohlig, R. T., Roberts, N., ... Johnson, C. L. (2020). Standard-space atlas of the viscoelastic properties of the human brain. *Human Brain Mapping*, 41(18), 5282– 5300. doi: 10.1002/hbm.25192.
- Hollis, L., Barnhill, E., Conlisk, N., Thomas-Seale,
 L. E. J., Roberts, N., Pankaj, P., & Hoskins, P.
 R. (2016). Finite element analysis to compare the accuracy of the direct and MDEV inversion algorithms in MR elastography. *IAENG International Journal of Computer Science*, 43(2), 137–146
- Honarvar, M., Sahebjavaher, R. S., Rohling, R., & Salcudean, S. E. (2017). A comparison of finite element-based inversion algorithms, local frequency estimation, and direct inversion approach used in MRE. *IEEE Transactions on Medical Imaging*, 36(8), 1686–1698. doi: 10. 1109/TMI.2017.2686388.
- Huston, J., Murphy, M. C., Boeve, B. F., Fattahi, N., Arani, A., Glaser, K. J., ... Ehman, R. L. (2016). Magnetic resonance elastography of frontotemporal dementia. *Journal of Magnetic Resonance Imaging*, 43(2), 474–478. doi: 10.1002/jmri.24977.
- Huston, J., Perry, A., Fattahi, N., Arani, A., Meyer, F., & Ehman, R. (2015). Magnetic resonance elastography demonstrates increased brain stiffness in normal pressure hydrocephalus. *Fluids* and *Barriers of the CNS*, *12*(Suppl 1), O38. doi: 10.1007/978-1-4939-1575-0.
- Johnson, C. L., Matijevich, E. S., Cullum, E. D., McGarry, M. D., Paulsen, K. D., Sutton, B. P., ... Olivero, W. C. (2016). MR elastography of intracranial tumors: Initial experience with highresolution imaging and nonlinear inversion, p. 1943. Proceedings of the 24th Annual Meeting of the ISMRM, Singapore, 2016. Concord, CA: International Society for Magnetic Resonance in Medicine.
- Johnson, C. L., Thompson, C. A., Sandro, B. M., Edwards, T. A., Hubbard, E. A., Klaren, R. E., ... Motl, R. W. (2017). Multiple sclerosis lesions are softer than surrounding white matter: An MR elastography study. *Proceedings of the* 25th Annual Meeting of the ISMRM, Honolulu, 2017. Concord, CA: International Society for Magnetic Resonance in Medicine.
- Kennedy, P., Barnhill, E., Gray, C., Brown, C., van Beek, E. J. R., Roberts, N., & Greig, C. A. (2020). Magnetic resonance elastography (MRE) shows significant reduction of thigh muscle stiffness in healthy older adults. *Gero-Science*, 42(1), 311–321. doi: 10.1007/s11357-019-00147-2.
- Kurt, M., Wu, L., Laksari, K., Ozkaya, E., Suar, Z. M., Lv, H., ... Wintermark, M. (2019). Optimization of a multifrequency magnetic resonance elastography protocol for the human brain. *Journal of Neuroimaging*, 29(4), 440– 446. doi: 10.1111/jon.12619.
- Kwon, O. I., Park, C., Nam, H. S., Woo, E. J., Seo, J. K., Glaser, K. J., ... Ehman, R. L. (2009). Shear modulus decomposition algorithm in magnetic

- resonance elastography. *IEEE Transactions on Medical Imaging*, 28(10), 1526–1533. doi: 10. 1109/TMI.2009.2019823.
- Latta, P., Gruwel, M. L. H., Debergue, P., Matwiy, B., Sboto-Frankenstein, U. N., & Tomanek, B. (2011). Convertible pneumatic actuator for magnetic resonance elastography of the brain. *Magnetic Resonance Imaging*, 29(1), 147–152. doi: 10.1016/j.mri.2010.07.014.
- Lee, C. U., Glockner, J. F., Glaser, K. J., Yin, M., Chen, J., Kawashima, A., ... Gloor, J. M. (2012). MR elastography in renal transplant patients and correlation with renal allograft biopsy—A feasibility study. *Academic Radiology*, 19(7), 834–841. doi: 10.1016/j.acra. 2012.03.003.
- Lipp, A., Skowronek, C., Fehlner, A., Streitberger, K. J., Braun, J., & Sack, I. (2018). Progressive supranuclear palsy and idiopathic Parkinson's disease are associated with local reduction of in vivo brain viscoelasticity. *European Radiology*, 28(8), 3347–3354. doi: 10.1007/s00330-017-5269-y.
- Lipp, A., Trbojevic, R., Paul, F., Fehlner, A., Hirsch, S., Scheel, M., ... Sack, I. (2013). Cerebral magnetic resonance elastography in supranuclear palsy and idiopathic Parkinson's disease. *NeuroImage: Clinical*, 3, 381–387. doi: 10.1016/j.nicl.2013.09.006.
- Liu, G. R., Gao, P. Y., Lin, Y., Xue, J., Wang, X. C., Sui, B.-B., ... Shen, H. (2009). Brain magnetic resonance elastography on healthy volunteers: A safety study. *Acta Radiologica*, 50(4), 423–429. doi: 10.1080/02841850902751681.
- Maharjan, S., Numano, T., Habe, T., Ito, D., Ueki, T., Igarashi, K., & Maeno, T. (2020). Directional filter, local frequency estimate and algebraic inversion of differential equation of psoas major magnetic resonance elastography. *Open Journal of Medical Imaging*, 10(01), 1–16. doi: 10.4236/ojmi.2020.101001.
- Manduca, A., Oliphant, T. E., Dresner, M. A., Lake,
 D. S., Greenleaf, J. F., & Ehman, R. L. (2002).
 Comparative evaluation of inversion algorithms for magnetic resonance elastography, p. 997-1000. Proceedings of the 2002 IEEE International Symposium on Biomedical Imaging. New York: Institute of Electrical and Electronics Engineers.
- Marticorena Garcia, S. R., Grossmann, M., Lang, S. T., Tzschätzsch, H., Dittmann, F., Hamm, B., ... Sack, I. (2018). Tomoelastography of the native kidney: Regional variation and physiological effects on in vivo renal stiffness. *Magnetic Resonance in Medicine*, 79(4), 2126–2134. doi: 10.1002/mrm.26892.
- McGarry, M. D. J., Van Houten, E. E. W., Perriez, P. R., Pattison, A. J., Weaver, J. B., & Paulsen, K. D. (2011). An octahedral shear strain-based measure of SNR for 3D MR elastography. *Physics in Medicine and Biology*, *56*(13), N153-64. doi: 10.1088/0031-9155/56/13/N02.
- McIlvain, G., Schwarb, H., Cohen, N. J., Telzer, E. H., & Johnson, C. L. (2018). Mechanical properties of the in vivo adolescent human brain.

- Developmental Cognitive Neuroscience, 34, 27–33. doi: 10.1016/j.dcn.2018.06.001.
- Meinhold, W., Ozkaya, E., Ueda, J., & Kurt, M. (2019). Tuneable resonance actuators for magnetic resonance elastography, no. DMD2019-3133. Proceedings for the 2019 Design of Medical Devices Conference: Frontiers in Biomedical Devices, Minneapolis, Minnesota, 2019.
 New York: American Society for Mechanical Engineers. doi: 10.1115/DMD2019-3313.
- Morisaka, H., Motosugi, U., Glaser, K. J., Ichikawa, S., Ehman, R. L., Sano, K., ... Onishi, H. (2017). Comparison of diagnostic accuracies of two- and three-dimensional MR elastography of the liver. *Journal of Magnetic Resonance Imaging*, 45(4), 1163–1170. doi: 10.1002/jmri.25425.
- Murphy, M. C., Huston, J., Jack, C. R., Glaser, K. J., Manduca, A., Felmlee, J. P., & Ehman, R. L. (2011). Decreased brain stiffness in Alzheimer's disease determined by magnetic resonance elastography. *Journal of Magnetic Resonance Imaging*, 34, 494–498. doi: 10.1002/jmri.22707.
- Murphy, M. C., Jones, D. T., Jack, C. R., Glaser, K. J., Senjem, M. L., Manduca, A., ... Huston, J. (2016). Regional brain stiffness changes across the Alzheimer's disease spectrum. *NeuroImage: Clinical*, *10*, 283–290. doi: 10.1016/j.nicl.2015. 12.007.
- Muthupillai, R., Rossman, P. J., Lomas, D. J., Greenleaf, J. F., Riederer, S. J., & Ehman, R. L. (1996). Magnetic resonance imaging of transverse acoustic strain waves. *Magnetic Resonance in Medicine*, 36(2), 266–274. doi: 10. 1002/mrm.1910360214.
- Namani, R., Wood, M. D., Sakiyama, S. E., & Bayly, P. V. (2009). Anisotropic mechanical properties of magnetically aligned fibrin gels measured by magnetic resonance elastography. *Journal of Biomechanics*, 42, 2047–2053. doi: 10.1016/j.jbiomech.2009.06.007.
- Neumann, W., Bichert, A., Fleischhauer, J., Stern, A., Figuli, R., Wilhelm, M., ... Zollner, F. G. (2018). A novel 3D printed mechanical actuator using centrifugal force for magnetic resonance elastography: Initial results in an anthropomorphic prostate phantom. *PLoS ONE*, *13*(10), 1–14. doi: 10.1371/journal.pone.0205442.
- Neumann, W., Lehnart, V. R., Vetter, Y., Bichert, A., Schad, L. R., & Zöllner, F. G. (2018). Coupled actuators with a mechanically synchronized phase during MR elastography: A phantom feasibility study. Concepts in Magnetic Resonance Part B: Magnetic Resonance Engineering, 48(4), 1–9. doi: 10.1002/cmr.b.21403.
- Numano, T., Kawabata, Y., Mizuhara, K., Washio, T., Nitta, N., & Homma, K. (2013). Magnetic resonance elastography using an air ball-actuator. *Magnetic Resonance Imaging*, 31(6), 939–946. doi: 10.1016/j.mri.2013.02.001.
- Ozkaya, E., Fabris, G., Macruz, F., Suar, Z. M., Abderezaei, J., Su, B., ... Kurt, M. (2021). Viscoelasticity of children and adolescent brains through MR elastography. *Journal of the Mechanical Behavior of Biomedical Mate-*

- *rials*, 115, 104229. doi: 10.1016/j.jmbbm.2020. 104229.
- Ozkaya, E., Triolo, E. R., Rezayaraghi, F., Abderezaei, J., Meinhold, W., Hong, K., ... Kurt, M. (2021). Brain-mimicking phantom for biomechanical validation of motion sensitive MR imaging techniques. *Journal of the Mechanical Behavior of Biomedical Materials*, 122, 104680. doi: 10.1016/j.jmbbm.2021.104680.
- Papazoglou, S., Hirsch, S., Braun, J., & Sack, I. (2012). Multifrequency inversion in magnetic resonance elastography. *Physics in Medicine and Biology*, *57*(8), 2329–2346. doi: 10.1088/0031-9155/57/8/2329.
- Papazoglou, S., Rump, J., Braun, J., & Sack, I. (2006). Shear wave group velocity inversion in MR elastography of human skeletal muscle. *Magnetic Resonance in Medicine*, *56*(3), 489–497. doi: 10.1002/mrm.20993.
- Pattison, A. J., Lollis, S. S., Perrinez, P. R., Weaver, J. B., & Paulsen, K. D. (2009). MR elastography of hydrocephalus. Proceedings of SPIE 7262, Medical Imaging 2009: Biomedical Applications in Molecular, Structural, and Functional Imaging, Lake Buena Vista, Florida, 72620A.
 Bellingham, Washington: International Society for Optics and Photonics. doi: 10.1117/12.811820.
- Perry, A., Graffeo, C. S., Fattahi, N., ElSheikh, M. M., Cray, N., Arani, A., ... Huston, J. (2017). Clinical correlation of abnormal findings on magnetic resonance elastography in idiopathic normal pressure hydrocephalus. World Neurosurgery, 99, 695–700. doi: 10.1016/j.wneu. 2016.12.121.
- Plewes, D. B., Bishop, J., Samani, A., & Sciarretta, J. (2000). Visualization and quantification of breast cancer biomechanical properties with magnetic resonance elastography. *Physics in Medicine and Biology*, 45, 1591–1610.
- Rossman, P., Glaser, K., Felmlee, J., & Ehman, R. (2003). Piezoelectric bending elements for use as motion actuators in MR elastography, p. 1075. Proceedings of 11th Annual Meeting of the ISMRM, Toronto, 2003. Concord, CA: International Society for Magnetic Resonance in Medicine.
- Rump, J., Klatt, D., Braun, J., Warmuth, C., & Sack, I. (2007). Fractional encoding of harmonic motions in MR elastography. *Magnetic Resonance* in *Medicine*, 57(2), 388–395. doi: 10.1002/mrm. 21152.
- Runge, J. H., Hoelzl, S. H., Sudakova, J., Dokumaci, A. S., Nelissen, J. L., Guenthner, C., ... Sinkus, R. (2019). A novel magnetic resonance elastography transducer concept based on a rotational eccentric mass: Preliminary experiences with the gravitational transducer. *Physics in Medicine and Biology*, 64(4), 045007. doi: 10.1088/1361-6560/aaf9f8.
- Sack, I., Beierbach, B., Wuerfel, J., Klatt, D., Hamhaber, U., Papazoglou, S., ... Braun, J. (2009). The impact of aging and gender on brain viscoelasticity. *NeuroImage*, 46(3), 652– 657. doi: 10.1016/j.neuroimage.2009.02.040.

- Sack, I., Bernarding, J., & Braun, J. (2002). Analysis of wave patterns in MR elastography of skeletal muscle using coupled harmonic oscillator simulations. *Magnetic Resonance Imaging*, 20(1), 95–104. doi: 10.1016/S0730-725X(02) 00474-5.
- Sack, I., Jöhrens, K., Würfel, J., & Braun, J. (2013). Structure-sensitive elastography: On the viscoelastic powerlaw behavior of *in vivo* human tissue in health and disease. *Soft Matter*, 9(24), 5672–5680. doi: 10.1039/c3sm50552a.
- Sack, I., Streitberger, K. J., Krefting, D., Paul, F., & Braun, J. (2011). The influence of physiological aging and atrophy on brain viscoelastic properties in humans. *PLoS ONE*, 6(9), e23451. doi: 10.1371/journal.pone.0023451.
- Shah, N. S., Kruse, S. A., Lager, D. J., Farell-Baril, G., Lieske, J. C., King, B. F., & Ehman, R. L. (2004). Evaluation of renal parenchymal disease in a rat model with magnetic resonance elastography. *Magnetic Resonance in Medicine*, 52(1), 56–64. doi: 10.1002/mrm.20101.
- Shi, Y., Gao, F., Li, Y., Tao, S., Yu, B., Liu, Z., ... Guo, Q. (2018). Differentiation of benign and malignant solid pancreatic masses using magnetic resonance elastography with spin-echo echo planar imaging and three-dimensional inversion reconstruction: A prospective study. *Eu*ropean Radiology, 28(3), 936–945. doi: 10. 1007/s00330-017-5062-y.
- Shi, Y., Glaser, K. J., Venkatesh, S. K., Ben-Abraham, E. I., & Ehman, R. L. (2015). Feasibility of using 3D MR elastography to determine pancreatic stiffness in healthy volunteers. *Journal of Magnetic Resonance Imaging*, 41(2), 369–375. doi: 10.1002/jmri.24572.
- Streitberger, K. J., Sack, I., Krefting, D., Pfüller, C., Braun, J., Paul, F., & Wuerfel, J. (2012). Brain viscoelasticity alteration in chronic-progressive multiple sclerosis. *PLoS ONE*, 7(1), e29888. doi: 10.1371/journal.pone.0029888.
- Streitberger, K. J., Wiener, E., Hoffmann, J., Freimann, F. B., Klatt, D., Braun, J., ... Sack, I. (2011). *In vivo* viscoelastic properties of the brain in normal pressure hydrocephalus. *NMR in Biomedicine*, 24(4), 385–392. doi: 10.1002/nbm.1602.
- Suga, M., Matsuda, T., Minato, K., Chihara, K., Oshiro, O., Okamoto, J., ... Takahashi, T. (2003). Measurement of in vivo local shear modulus using MR elastography multiple-phase patchwork offsets. *IEEE Transactions on Biomedical Engineering*, 50(7), 908–915. doi: 10.1109/TBME. 2003.813540.
- Suga, M., Matsuda, T., Minato, K., Oshiro, O., Chihara, K., Okamoto, J., ... Takahashi, T. (2001). Measurement of in-vivo local shear modulus by combining multiple phase offsets MR elastography. Studies in Health Technology and Informatics, 84, 933–937. doi: 10.3233/978-1-60750-928-8-933.
- Triolo, E., Pionteck, A., Alipour, A., Khegai,
 O., Kennedy, P., Balchandani, P., & Kurt, M.
 (2021). Development and validation of an ultrahigh field compatible MR elastography actua-

- tor. Proceedings of the Summer Biomechanics, Bioengineering and Biotransport Conference, SB³C2021-325. Lancaster, Pennsylvania: SB³C Foundation.
- Tse, Z. T. H., Janssen, H., Hamed, A., Ristic, M., Young, I., & Lamperth, M. (2009). Magnetic resonance elastography hardware design: A survey. *Proceedings of the Institution of Mechanical Engineers, Part H: Journal of Engineering in Medicine*, 223(4), 497–514. doi: 10.1243/09544119JEIM529.
- Uffmann, K., Abicht, C., Grote, W., Quick, H. H., & Ladd, M. E. (2002). Design of an MR-compatible piezoelectric actuator for MR elastography. Concepts in Magnetic Resonance Part B: Magnetic Resonance Engineering, 15(4), 239–254. doi: 10.1002/cmr.10045.
- Uffmann, K., Abicht, C., Quick, H. H., Ulbrich, H., & Ladd, M. E. (2001). Characterization of an electromagnetic actuator for MR elastography, p. 1635. *Proceedings of the 9th Annual Meeting of the ISMRM*, *Glasgow, Scotland*, 2001. Concord, CA: International Society for Magnetic Resonance in Medicine.
- Van Houten, E. E. W., Doyley, M. M., Kennedy, F. E., Weaver, J. B., & Paulsen, K. D. (2003). Initial in vivo experience with steadystate subzone-based MR elastography of the human breast. *Journal of Magnetic Reso*nance Imaging, 17(1), 72–85. doi: 10.1002/jmri. 10232.
- Van Houten, E. E. W., Miga, M. I., Weaver, J. B., Kennedy, F. E., & Paulsen, K. D. (2001). Threedimensional subzone-based reconstruction algorithm for MR elastography. *Magnetic Resonance in Medicine*, 45(5), 827–837. doi: 10. 1002/mrm.1111.
- Venkatesh, S. K., Yin, M., & Ehman, R. L. (2013). Magnetic resonance elastography of liver: Technique, analysis and clinical applications. *Journal of Magnetic Resonance Imaging: JMRI*, 37(3), 544–555. doi: 10.1002/jmri. 23731.Magnetic.
- Wassenaar, P. A., Eleswarpu, C. N., Schroeder, S. A., Mo, X., Raterman, B. D., White, R. D., & Kolipaka, A. (2016). Measuring age-dependent myocardial stiffness across the cardiac cycle using MR elastography: A reproducibility study. *Magnetic Resonance in Medicine*, 75(4), 1586–1593. doi: 10.1002/mrm.25760.
- Wuerfel, J., Paul, F., Beierbach, B., Hamhaber, U., Klatt, D., Papazoglou, S., ... Sack, I. (2010). MR-elastography reveals degradation of tissue integrity in multiple sclerosis. *NeuroImage*, 49(3), 2520–2525. doi: 10.1016/j.neuroimage. 2009.06.018.
- Xu, L., Lin, Y., Xi, Z. N., Shen, H., & Gao, P. Y. (2007). Magnetic resonance elastography of the human brain: A preliminary study. *Acta Radiologica*, 48(1), 112–115. doi: 10. 1080/02841850601026401.
- Yin, M., Manduca, A., Romano, A. J., Glaser, K. J., Drapaca, C. S., Lake, D. S., & Ehman, R. L. (2007). 3-D local frequency

- estimation inversion for abdominal MR elastography. *Proceedings of the 15th Annual Meeting of the ISMRM, Berlin, 2007.* Concord, CA: International Society for Magnetic Resonance in Medicine.
- Yin, M., Rouviere, O., Glaser, K. J., & Ehman, R. L. (2008). Diffraction-biased shear wave fields generated with longitudinal magnetic resonance elastography drivers. *Magnetic Resonance Imaging*, 26, 770–780. doi: 10.1016/j. mri.2008.01.019.
- Yin, Z., Kearney, S. P., Magin, R. L., & Klatt, D. (2017). Concurrent 3D acquisition of diffusion tensor imaging and magnetic resonance elastography displacement data (DTI-MRE): Theory and in vivo application. Magnetic Resonance in

- *Medicine*, 77(1), 273–284. doi: 10.1002/mrm. 26121.
- Zhang, J., Green, M. A., Sinkus, R., & Bilston, L. E. (2011). Viscoelastic properties of human cerebellum using magnetic resonance elastography. *Journal of Biomechanics*, 44(10), 1909–1913. doi: 10.1016/j.jbiomech.2011.04.034.
- Zheng, Y., Li, G., Chen, M., Chan, Q. C. C., Hu, S. G., Zhao, X. N., ... Yang, E. S. (2007). Magnetic resonance elastography with twin pneumatic drivers for wave compensation, pp. 2611–2613. Proceedings of the 29th Annual International Conference of the IEEE Engineering in Medicine and Biology. New York: Institute of Electrical and Electronics Engineers. doi: 10. 1109/IEMBS.2007.4352864.